Disentangling Projected Stationary Wave Changes: Implications for Future Drying of the Mediterranean Region

BENNY KELLER,[a,b] CHAIM I. GARFINKEL,[b] AND EDWIN P. GERBER[c]

[a] *Atmospheric, Oceanic and Planetary Physics, Department of Physics, University of Oxford, Oxford, United Kingdom*
[b] *Institute of Earth Sciences, The Hebrew University of Jerusalem, Jerusalem, Israel*
[c] *Courant Institute of Mathematical Sciences, New York University, New York, New York*

(Manuscript received 11 November 2024, in final form 10 June 2025, accepted 30 June 2025)

ABSTRACT: An intermediate-complexity general circulation model is used to disentangle changes in the large-scale zonally asymmetric circulation in response to rising greenhouse gases. Particular focus is on the anomalous ridge that develops over the Mediterranean in future climate projections, directly associated with reduced winter precipitation over the region. Specifically, we examine changes in stationary waves forced by land–sea contrast, horizontal oceanic heat fluxes, and orography, following a quadrupling of CO_2. The stationary waves associated with these three drivers depend strongly on the climatological state, precluding a linear decomposition of their responses to warming. However, our modeling framework still allows a process-oriented approach to quantify the key drivers and mechanisms of the response. A combination of three similarly important mechanisms is found responsible for the rain-suppressing ridge. The first is part of a global response to warming: elongation of intermediate-scale stationary waves in response to strengthened subtropical winds aloft, previously found to account for hydroclimatic changes in southwestern North America. The second is regional: a downstream response to the North Atlantic warming hole and enhanced warming of the Eurasian landmass relative to the Atlantic Ocean. A third contribution to the Mediterranean Ridge is a phase shift of planetary wave 3, primarily associated with an altered circulation response to orographic forcing. Reduced land–sea contrast in the Mediterranean basin, previously thought to contribute substantially to Mediterranean drying, has a negligible effect in our integrations. This work offers a mechanistic analysis of the large-scale processes governing projected Mediterranean drying, lending increased understanding and credibility to climate model projections.

KEYWORDS: Mediterranean Sea; North Atlantic Ocean; Atmospheric circulation; Stationary waves; Climate change; Idealized models

1. Introduction

Changes in regional precipitation and hydroclimate are among the most impact-relevant aspects of global warming. Rising temperatures are expected to cause a zonal-mean drying of the subtropical dry regions and wetting of the tropical and mid–high-latitude wet regions, as atmospheric moisture holding capacity increases (Held and Soden 2006) and moisture transport intensifies (Seager et al. 2010). This zonal-mean pattern, however, is not representative of conditions in any specific region. The precipitation response varies strongly with longitude, due to the strong zonal structure of storm tracks and stationary waves, i.e., the time-mean zonal deviations from the zonal-mean flow, and their associated quasi-stationary highs and lows. This zonal structure is particularly pronounced in the Northern Hemisphere (NH; Simpson et al. 2014). Uncertainty in the projected response of stationary waves to increased CO_2 leads to large intermodel spread in precipitation projections in the extratropics (Neelin et al. 2013; Garfinkel et al. 2020a; Wills et al. 2019; Elbaum et al. 2022). Therefore, accurate future precipitation projections depend upon an improved understanding of the midlatitude large-scale circulation response to warming and upon the ability of models to resolve key processes driving the change.

The Mediterranean region has been termed a climate change "hotspot" (Giorgi 2006; Cos et al. 2022) due to its particular sensitivity to rising concentrations of greenhouse gases (GHGs) in global climate models (GCMs). As GHG concentrations rise, models project, with strong agreement, a decrease in winter precipitation in the Mediterranean basin, particularly in the southeast of the region (Giorgi and Lionello 2008; Garfinkel et al. 2020a), that is more pronounced than anywhere else in the NH subtropics. The large reduction in precipitation in the region is associated with another climate feature projected robustly across GCMs: the formation of an anomalous surface anticyclone over the Mediterranean basin in winter months, accompanied by an upper-level ridge (Giorgi and Lionello 2008). The magnitude of the surface anticyclone is strongly correlated with the regional winter precipitation decline across CMIP5 models (Zappa et al. 2015b). As opposed to summer drying, reduced Mediterranean winter precipitation is projected only when circulation changes are included (Brogli et al. 2019).

Denotes content that is immediately available upon publication as open access.

Supplemental information related to this paper is available at the Journals Online website: https://doi.org/10.1175/JCLI-D-24-0659.s1.

Corresponding author: Benny Keller, benjamin.keller@new.ox.ac.uk

DOI: 10.1175/JCLI-D-24-0659.1

It has long been assumed that the anomalous winter Mediterranean high drives the projected drying by increasing atmospheric stability in the region and suppressing Mediterranean cyclones (Giorgi and Lionello 2008). Zappa et al. (2015a) found that future Mediterranean drying is strongly related to a decrease in the number of Mediterranean cyclones, further amplified in the eastern Mediterranean by a reduction in the amount of precipitation generated by individual cyclones. Future heavy rainfall events in the eastern Mediterranean are projected to yield reduced rainfall, mainly due to a decrease in the rain area, despite an increased rain rate (Armon et al. 2022). In addition, enhanced dry air advection from the Sahara Desert appears to be a main driver of the drying in the western Mediterranean (Tuel et al. 2021a). Yet the question remains as to why the anomalous rain-suppressing high pressure develops in the first place, and this is the subject of our study.

After reviewing mechanisms potentially relevant for Mediterranean drying in the literature (section 2), the simulation environment and experiments performed in this study are introduced in section 3. The results of our experiments and the role of individual stationary wave forcings for projected Mediterranean drying are then presented in section 4. The various stationary wave drivers exhibit unique responses to warming and contribute differently to projected Mediterranean drying. However, they are found to interact nonadditively, pointing at substantial nonlinearity. Therefore, a process-oriented approach follows: A wavenumber decomposition of the stationary wave response to warming is performed in sections 5a and 5b; an analysis of the zonally anomalous thermodynamic budget is shown in section 5c; and the role of regional land–sea contrast components is isolated in section 5d, by manipulating the model landmask. Finally, the various mechanisms explaining winter Mediterranean drying are re-evaluated in light of our results in section 6, and our conclusions are summarized in section 7.

2. Background and theory

Various large-scale circulation changes have been proposed as drivers of the Mediterranean drying, including a weakening of the Mediterranean storm track (Lionello and Giorgi 2007; Zappa et al. 2015a) and a poleward shift of the Hadley cell, associated with a corresponding shift of the North Atlantic storm track (Scheff and Frierson 2012). As yet, a satisfactory and universally accepted explanation has yet to be found. The Hadley cell and storm-track shifts occur on a slower time scale than the projected precipitation decrease in the subtropics (He and Soden 2017), and the intermodel spread in zonal-mean changes in the Hadley cell is uncorrelated with precipitation changes in the eastern Mediterranean (Garfinkel et al. 2020a). Moreover, Byrne and O'Gorman (2015) found that modifying the "wet-gets-wetter, dry-gets-drier" scaling (Held and Soden 2006) to account for changes in horizontal temperature gradients improves estimates of regional changes in $P - E$, especially over land. Therefore, the zonally pronounced drying in the Mediterranean and the correlated change in sea level pressure (SLP) require an explanation involving zonally asymmetric factors.

Several zonally sensitive mechanisms of potential relevance to the Mediterranean drying have been put forward. Simpson et al. (2016) show that future precipitation trends over western North America are regulated by the changes in the pattern of NH stationary waves. Strengthened zonal-mean westerlies in the subtropical upper troposphere, associated with the warming of the tropical upper troposphere (a robust and well-studied climate change feature), lead to a lengthening of intermediate-scale zonally propagating stationary waves. This lengthening results in a shift of the meridional winds in the Pacific Ocean, directly altering precipitation patterns in the western United States via drying northerlies and wetting southerlies. The CMIP5 multimodel mean response analyzed in Simpson et al. (2016) suggests a downstream effect of the Pacific lengthening over the Atlantic Ocean and Eurasia. However, models with a larger response over North America do not all show the same over the Mediterranean. Moreover, different processes and time scales of the climate response to increasing GHGs have been found to constrain hydroclimate changes in the Southwest United States versus the Mediterranean (Zappa et al. 2020). The relevance of this mechanism for Mediterranean drying will be investigated in section 5a.

Gervais et al. (2019) studied the circulation response to an idealized North Atlantic warming hole (NAWH), a warming deficit in the subpolar North Atlantic sea surface temperatures seen both in twentieth-century observations (Rahmstorf et al. 2015) and in future climate projections (Drijfhout et al. 2012; Gervais et al. 2018). They find that the enhanced sea surface temperature (SST) gradient caused by the NAWH leads to a stronger subpolar SST front. This generates increased surface baroclinic transient eddy activity that propagates vertically and downstream. In the upper troposphere, this eddy activity enhances the midlatitude eddy-driven jet well downstream of the NAWH. Consistent with geostrophic balance, this is associated with equivalent-barotropic increased (reduced) geopotential height equatorward (poleward) of the jet change. The relevance of this regional response to warming for the Mediterranean climate downstream will be discussed in sections 5c and 6b.

Tuel and Eltahir (2020) argue that a weakening of the land–sea temperature gradient in the Mediterranean region accounts for a considerable fraction of the projected drying in the region. Specifically, enhanced warming over land compared to sea, expected as CO_2 concentrations rise (Sutton et al. 2007), reduces the winter temperature gradient between the Mediterranean Sea and the land surrounding it. The geostrophically balanced response to the decreased gradient leads to a surface anticyclonic circulation, suppressing winter precipitation. The importance of this mechanism will be assessed in section 5d.

Finally, Zappa et al. (2020) propose that in regions where atmospheric circulation is important for hydroclimate changes, the precipitation response to warming should be characterized using three time scales: a rapid adjustment to the change in radiative forcing, a fast SST-driven response, and a slow SST-driven response. The warming pattern differs for each time scale, and each induces different circulation changes. They find that the precipitation decline in the Mediterranean evolves in

quasi-equilibrium with GHG forcing and is the largest in the fast SST-driven response. Moreover, only in response to this time scale does a strong surface anticyclonic circulation form. This is not the case in all Mediterranean-like regions. In the U.S. West Coast, for example, where a significant wetting is projected as GHG concentrations rise (Neelin et al. 2013), the full hydroclimate response reaches its maxima only after GHG concentrations stabilize and is largely due to the slow SST-driven response. This framework and the strong decline in Mediterranean rainfall in the fast SST-driven response informed the design of the experiments performed in this study.

3. Data and methods

All simulations presented in this paper are run using the Model of an Idealized Moist Atmosphere (MiMA), an intermediate-complexity general circulation model (Jucker and Gerber 2017; Garfinkel et al. 2020c,b). A key advantage of the model is that it captures the interplay between atmospheric dynamics, radiation, and moisture, but with idealizations that allow mechanisms to be isolated. The model simulates the primitive equations on the sphere at moderate resolution, generating realistic synoptic variability. It uses the RRTMG radiation scheme, developed by Atmospheric and Environmental Research (AER) (Iacono et al. 2008), which allows us to incorporate the radiative impacts of ozone and water vapor into the model. The hydrological cycle and a boundary layer scheme based on Monin–Obukhov similarity theory are incorporated following Frierson et al. (2006). The atmosphere is coupled to a mixed layer ocean and both idealized surface topography and realistic topography configurations are used. The depth of the mixed layer can be varied to approximate land–sea contrast (LSC), and steady horizontal ocean heat transport (OHT) can be imposed to approximate heat transport by ocean currents (Garfinkel et al. 2020c,b). There is no seasonal vertical mixing of heat in the model.

The flexible setup of the physical parameterizations allows one to perturb the climate state without extensive retuning. Specifically, the addition of orography, LSC, and OHT can be switched on or off independently. Hence, in a single modeling framework, we can alternately simulate a moist zonally symmetric aquaplanet or a model that can compete with CMIP6 models in its ability to simulate both the zonal-mean and zonal asymmetries of the large-scale atmospheric circulation (Garfinkel et al. 2020c,b), as well as the desired states in between. For example, the ability to "turn off LSC" but otherwise retain all other stationary wave drivers allows us to confirm/deny the importance of LSC changes, and among those the relative Mediterranean cooling theory (Tuel and Eltahir 2020), for the circulation response over the Mediterranean. We are thus able to isolate, and subsequently synthesize, fundamental physical processes that regulate the extratropical circulation response to GHGs and, more specifically, the response in the Mediterranean basin. Finally, this idealized model captures the key processes that drive stationary waves, and the linear and nonlinear interaction between them (Garfinkel et al. 2020c).

Many past studies of the response of stationary waves to warming have used stationary wave models linearized about a prescribed zonal-mean basic state (Stephenson and Held 1993; Joseph et al. 2004; Freitas and Rao 2014; Simpson et al. 2016) to understand the response. Such a framework allows one to differentiate between the contribution of an altered zonal-mean basic state versus changes in the zonally asymmetric wave forcings, such as an altered diabatic heating source. Some have found that the response to warming is dominated by the changes in zonally asymmetric forcing (Stephenson and Held 1993; Freitas and Rao 2014), while others concluded that the zonal-mean basic state is an important (Joseph et al. 2004), if not the primary driver (Simpson et al. 2016), of the response. A limitation of our model is that we cannot distinguish these mechanisms or account for the relative contribution of the basic state versus the zonally asymmetric diabatic heating for the stationary wave response to warming, as the model solves the full nonlinear primitive equations, with moisture. This limitation also has its advantages, however, as the zonal asymmetric diabatic tendencies, and to a smaller extent, the zonal-mean flow, are themselves modified by stationary waves (Held et al. 2002), interactions that are captured by our model.

a. *Experiments*

Table 1 lists the experiments analyzed in this paper. For all configurations, we first run an experiment with contemporary CO_2 concentrations, set to a constant 390 ppm (hereafter $1xCO_2$). For this experiment, we retain the last 37 years after discarding 28 years of spinup. Next, we spin off from the 29th year of the $1xCO_2$ simulation and impose an instantaneous quadrupling of CO_2 concentrations (1560 ppm; hereafter $4xCO_2$), and run for an additional 40 years. We examine the last 37 years of this $4xCO_2$ run. The rationale behind this setup is that all $1xCO_2$ experiments begin with an equilibrated temperature field, while all $4xCO_2$ experiments simulate the "fast ocean" response to rising GHGs, similar to the fast SST response responsible for Mediterranean drying in Zappa et al. (2020, see section 2). This short-to-intermediate term response is also the one our model is most suited to, as it lacks a deep ocean. All experiments are run at a horizontal resolution of triangular truncation 42 (T42) with 40 vertical pressure levels. The results for each simulation are averaged over 37 equally weighted years. All results shown in this paper focus on the winter months, chosen to be December–March (DJFM).

The precipitation, temperature, and geopotential height response to the quadrupling of CO_2 are first examined in a realistic climate simulation (experiment 1 in Table 1; hereafter ALL), with all three stationary wave drivers activated: orography, horizontal ocean heat transport, and land–sea contrast. When imposed together, these three forcings reproduce the time-mean geopotential height field and its zonal deviations (i.e., the stationary waves), as well as in CMIP5 models (Garfinkel et al. 2020c). Hence, we refer to them as the building blocks of stationary waves.

TABLE 1. MiMA experiments, with "Y" indicating that forcing is on and "N" indicating that forcing is off. The full nonlinear response to any single forcing is the difference between the realistic simulation (experiment 1) and a single negative experiment, i.e., an experiment in which the examined forcing is off. In experiments 5–8, the landmask was manipulated, yet all stationary wave forcings are activated.

Name	Experiment num.	Orography	LSC	OHFs	Landmask manipulation
Aquaplanet	0	N	N	N	N
ALL	1	Y	Y	Y	N
No LSC	2	Y	N	Y	N
No OHT	3	Y	Y	N	N
No orography	4	N	Y	Y	N
No Mediterranean Sea	5	Y	Y	Y	Mediterranean Sea changed to land
No North Africa and no Europe	6	Y	Y	Y	Europe and North Africa changed to sea
No Asia	7	Y	Y	Y	Eurasian continent changed to sea
No North America	8	Y	Y	Y	North America changed to sea

To evaluate the change in the wave forced by each building block as GHG concentrations rise, we run three simulations in which one is deactivated (experiments 2–4 in Table 1) and compare the result to ALL. This yields the "full" nonlinear response, following the terminology of Held et al. (2002), as opposed to the "isolated" nonlinear response, which corresponds to the perturbation obtained by imposing a given building block on an initially zonally symmetric state. This guarantees that the forcing attributed to each building block represents not only the change in zonal asymmetries it causes in isolation but also the linear and nonlinear interaction with the background state set up by the other two forcings. We acknowledge that OHT and SST asymmetry, important stationary wave drivers, are themselves affected by the atmospheric stationary wave structure, as they amplify the SST asymmetry through heat and moisture advection. We cannot differentiate these two processes in our model. It should be noted that activating/deactivating the east–west OHT in our model setup does not add net heat to the ocean.

A zonally symmetric aquaplanet simulation is included for reference (experiment 0 in Table 1). In experiments 5–8, the landmask is manipulated, allowing us to evaluate the role of regional LSC elements for the stationary wave response.

The difference between "land" and "ocean" in our experiments is in the heat capacity, surface friction, and moisture availability. For the realistic experiment, observed orography is applied, as resolved by the model at T42. In experiments in which the effect of orography is deactivated, a uniform height of just 15 (m) is used over land areas. OHT includes idealized Pacific and Atlantic Ocean tropical warm pools and an approximation of NH western boundary currents: the Gulf Stream in the western Atlantic and Kuroshio in the western Pacific. In experiments in which OHT is deactivated, there is still a simple representation of zonally uniform tropical meridional ocean heat transport. See the online supplemental material for further details on how LSC and ocean heat flux (OHF) are implemented in our experiments.

It should be noted that orographic stationary waves change in response to $4xCO_2$ due to the changes in the mean flow that interacts with the mountains, while the boundary forcing remains fixed. However, for LSC and OHT-forced waves, the surface forcing of the waves changes, in addition to the altered mean flow.

b. Metrics

We quantify the planetary stationary wave as the time-mean deviations from the zonal mean of the geopotential height field, as it has been strongly associated with Mediterranean drying in past studies (Giorgi and Lionello 2008; Zappa et al. 2015b). The stationary wave response in the main experiments in this paper is essentially the same if diagnosed by the meridional wind v^* (see Figs. S2–S4).

Planetary-scale stationary waves are principally forced near the surface and then propagate vertically upward (Charney and Drazin 1961). Winter NH stationary waves are largely barotropic, with the largest anomalies in the mid–upper troposphere. Therefore, we present the changes in the stationary waves at 230 hPa, although results are similar lower down.

c. Zonally anomalous steady-state thermodynamic budget

Stationary wave amplitude and structure depend greatly upon the meridional temperature gradient and zonal asymmetries in diabatic heating (Charney and Drazin 1961; Hoskins and Karoly 1981), both of which are expected to change in response to warming. Extratropical diabatic heating is balanced primarily by horizontal advection rather than by adiabatic heating from vertical motion (Hoskins and Karoly 1981; Held 1983). If the horizontal advection term includes a contribution from meridional temperature advection, then the implied meridional winds necessitate a stationary wave response. The amplitude of this response is sensitive to the magnitude of $d\theta/dy$, and hence, altered $d\theta/dy$ also affects the net stationary wave response. Specifically, a weakening (in absolute magnitude) of the meridional temperature gradient $d\theta/dy$ requires a stronger stationary wave, i.e., meridional wind $\overline{v}$, to restore balance, absent any other changes (Wills et al. 2019; Held et al. 2002). Moreover, changes in the zonal temperature gradient $d\theta/dx$ also force changes in meridional temperature advection.

This effect can be interpreted and quantified through the zonally anomalous steady-state thermodynamic budget, which following Wills and Schneider (2018) and Garfinkel et al. (2020c) can be written as

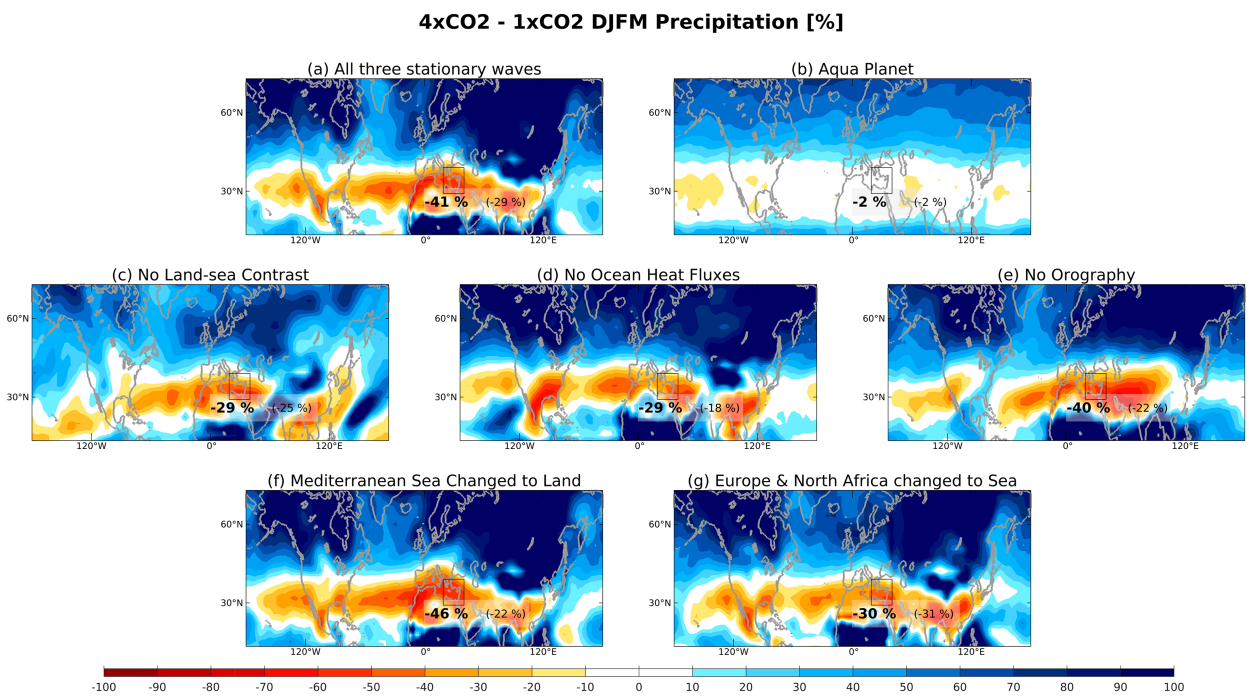

FIG. 1. DJFM percentage change in precipitation $4xCO_2$–$1xCO_2$ for (a) ALL, the realistic configuration with all three stationary wave building blocks activated; (b) aquaplanet configuration with none of the building blocks; (c) no LSC, orography, and OHT only; (d) "no OHT," orography, and LSC only; (e) "no orography," LSC, and OHT only; (f) Mediterranean Sea changed to land; (g) Europe and North Africa changed to sea. Noted in bold on each subplot is the precipitation change in the eastern half of the Mediterranean basin (29°–40°N, 19°–40°E; outlined). In brackets is the zonal-mean drying for the same latitude band (29°–40°N).

$$\left(\underbrace{\overline{u}\frac{\partial\overline{\theta}}{\partial x}}_{\text{zonal advection}} + \overbrace{\overline{v}\frac{\partial\overline{\theta}}{\partial y}}^{\text{meridional advection}} + \underbrace{\overline{\omega}\frac{\partial\overline{\theta}}{\partial p}}_{\text{vertical term}}\right)^{*} + \overbrace{\nabla\cdot(\overline{\mathbf{v}'\theta'})^{*}}^{\text{transient eddies}} - \underbrace{\overline{Q}^{*}}_{\text{diabatic terms}} = 0, \quad (1)$$

where θ is the potential temperature; ω is the vertical pressure velocity; and Q is the diabatic heating due to latent heat release, radiation, and other nonconservative processes. Time means are denoted by bars, deviations from a zonal mean are denoted by an asterisk, and deviations from the time mean are denoted by primes. The first three terms on the LHS mark the temperature advection by the time-mean flow and $\nabla\cdot(\overline{\mathbf{v}'\theta'})^{*}$ is the temperature fluxes by transient eddies ($\mathbf{v}$ is a vector that has u, v, and ω components). To further illustrate the forcing of stationary waves, the thermodynamic budget [Eq. (2)] can be rearranged, as in Garfinkel et al. (2020c):

$$\left(\overline{v}\frac{\partial\overline{\theta}}{\partial y}\right)^{*} = -\left(\overline{u}\frac{\partial\overline{\theta}}{\partial x} + \overline{\omega}\frac{\partial\overline{\theta}}{\partial p}\right)^{*} - \nabla\cdot(\overline{\mathbf{v}'\theta'})^{*} + \overline{Q}^{*}. \quad (2)$$

The budget in Eq. (2) will be utilized in section 5c to gain further understanding of our results and particularly, of the stationary wave response to changes in the temperature spatial pattern.

We show temperature changes and the thermodynamic budget at 700 hPa. Results are similar in the upper troposphere (with the transient term slightly less important while the time-mean advection terms are somewhat more important); however, the connection to the surface forcing is clearer at this level.

4. The precipitation and circulation response to warming in the Mediterranean region and the role of stationary wave building blocks

The change in winter precipitation following a quadrupling of CO_2 concentrations is presented in Fig. 1 for experiments 0–6, given in Table 1. The percentage noted in bold on each figure quantifies the precipitation change in the eastern half of the Mediterranean basin (29°–40°N, 19°–40°E), projected to experience the most enhanced winter drying (Giorgi and Lionello 2008; Brogli et al. 2019). A decrease in precipitation is found over most of the subtropics in the realistic configuration with all three forcings activated (ALL, Fig. 1a). A strong and zonally pronounced drying is found over the Mediterranean Sea and the land surrounding it, with a difference in the magnitude between the northwest and southeast of the basin, consistent with previous studies (Giorgi and Lionello 2008; Brogli et al. 2019; Tuel and Eltahir 2020).

In the zonally symmetric aquaplanet configuration, with all three stationary wave drivers deactivated, there is only moderate drying in the subtropics (Fig. 1b). In the zonal mean, ALL exhibits substantially more drying: 29% between 29°

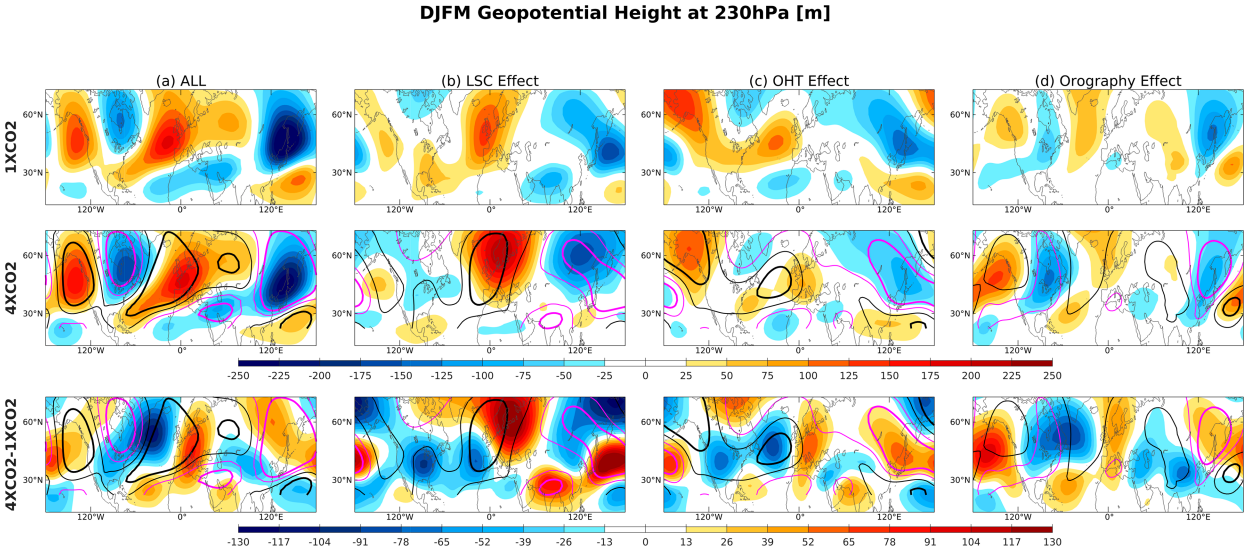

FIG. 2. DJFM zonally anomalous geopotential height at 230 hPa for (a) ALL, the realistic configuration with all three stationary wave building blocks activated; (b) ALL–no LSC, isolating the LSC effect; (c) ALL–no OHT, isolating the OHT effect; (d) ALL–no orography, isolating the orography effect. (top) The $1xCO_2$ climatology (shading). (middle) The $4xCO_2$ climatology (shading) compared to the $1xCO_2$ climatology (contours). (bottom) The $4xCO_2$–$1xCO_2$ anomaly (shading) compared to the $1xCO_2$ climatology (contours). The contours indicate the geopotential height of ±25 and ±75 m in $1xCO_2$ climatology. Black/magenta contours mark positive/negative. The zonal-mean geopotential height at each latitude is subtracted to form deviations from the zonal-mean, and we then time average each of the $1xCO_2$ and $4xCO_2$ responses, before computing their difference.

and 40°N versus just 2% in the aquaplanet. While all three building blocks encourage subtropical drying, pronounced drying in the Mediterranean in particular is tied to changes in the OHT- and LSC-driven waves (Figs. 1c,d). When either of these two building blocks is deactivated, approximately 30% less Mediterranean drying is found compared to ALL. In contrast, when orographic stationary waves are removed, there is little change in the precipitation response to warming in the region (Fig. 1e).

The magnitude and pattern of projected subtropical precipitation changes vary widely across models and are sensitive to the convection scheme and parameterization (Garfinkel et al. 2024). Therefore, we focus the rest of this paper on the changes in the geopotential height associated with Mediterranean drying, a variable with higher reliability in GCMs in general, and in our idealized model in particular (Garfinkel et al. 2020c).

Figure 2 displays the zonally asymmetric response of the upper-tropospheric geopotential height field to a quadrupling of CO_2. The stationary wave in ALL with $1xCO_2$ is very similar to that in the historical simulation of CMIP5 models, as detailed by Garfinkel et al. (2020c). The stationary wave change in response to $4xCO_2$ in ALL is also very similar to the end-of-century projections in the RCP8.5 scenario averaged over CMIP5 models (Wills et al. 2019). Some discrepancies are found in the east Pacific and along the southwestern North American coast. These are regions where precipitation projections are less robust due to model-based uncertainty (Seager et al. 2024).

The first-order NH stationary wave response to warming is a downstream shift in the phase of the midlatitude wave (Fig. 2a, lower panel), consistent with CMIP5 model-mean response in RCP8.5 (Wills et al. 2019). This response is more pronounced, and with larger meridional span, in the Atlantic versus the Pacific sector. The western North American Ridge and Hudson Bay trough strengthen with warming, while the East Asian low weakens slightly. Focusing on the Mediterranean region, the climatological $1xCO_2$ east Atlantic Ridge shifts eastward in response to $4xCO_2$ while maintaining its amplitude, generating a strong anticyclonic anomaly across the center of the Mediterranean Sea and stretching north over western-central Europe, consistent with previous studies (Giorgi and Lionello 2008; Wills et al. 2019; Tuel and Eltahir 2020).

We next decompose the stationary wave response to warming into each of its three drivers (Figs. 2b–d). The response of the LSC-forced stationary wave (Fig. 2b) is complex, as expected given the detailed spatial pattern of the SST response to warming (Zappa et al. 2020). In the Euro-Atlantic sector, the North Atlantic Ridge strengthens and shifts downstream and poleward, resulting in a strong positive anomaly over northern Europe.

The OHT-forced stationary wave (Fig. 2c) weakens in $4xCO_2$. In the North Atlantic, the wave also shifts downstream, generating a positive anomaly over the Mediterranean, similar in its spatial pattern to that in ALL, and accounting for approximately 65% of its amplitude. The orography-forced stationary wave strengthens over the Pacific Ocean and North America and weakens over Asia in $4xCO_2$ (Fig. 2d). The wave driven by the Himalayas and Tibetan Plateau weakens, while the wave forced by the Rocky Mountains strengthens and expands zonally. The latter results in a positive anomaly downstream over northwestern Europe and the western Mediterranean Sea,

which also contributes to the response in ALL (approximately 35% of the response in Fig. 2a).

Changes in the OHT-driven stationary wave account for a significant part of the amplitude and location of the anomalous Mediterranean Ridge, with a more modest contribution from the orography-driven wave. The LSC-driven wave does not generate a clear anticyclonic signal above the Mediterranean but does so further north, affecting the final position of the ridge (Fig. S6b further clarifies this point, showing the location of the ridge in the "no LSC" simulation).

An important caveat is that the sum of the responses to each of the three building blocks does not yield the total stationary wave in the $1xCO_2$ (as shown by Garfinkel et al. 2020c), $4xCO_2$, or $4xCO_2$–$1xCO_2$ rows in Fig. 2. A similar result is found when considering the sum of the precipitation responses to each of the building blocks in Fig. 1. This nonadditivity highlights the substantial nonlinear interactions in the system. Therefore, we cannot simply reduce the problem to a linear combination of forcings. For this reason, we do not consider the isolated response to each of the building blocks in this paper. This also implies that mechanisms found in linearized stationary wave models may not translate to a more complex GCM, let alone the real atmosphere. In light of this nonadditive dynamic, the decomposition of the stationary wave response to the relative contribution of the basic state and the zonally asymmetric diabatic heating, as performed in studies with linear baroclinic stationary wave models (Stephenson and Held 1993; Joseph et al. 2004; Freitas and Rao 2014), is not very meaningful.

5. A process-oriented assessment of the circulation response to warming over the Mediterranean

Despite the nonadditivity of the precipitation and circulation responses to stationary wave building blocks in a warmer climate, a reductionist, process-oriented approach can still identify and quantify key drivers and mechanisms of the response. To do so, in the following section, we perform a wavenumber decomposition of the stationary wave response to warming (sections 5a,b), utilize the zonally anomalous steady-state thermodynamic balance to diagnose the stationary wave surface forcing upstream of the Mediterranean (section 5c), and explore the role of changes in regional LSC components (section 5d).

We first distinguish between large-scale ($k \leq 3$) and intermediate-scale ($k \geq 4$) stationary waves. The former propagate more meridionally, while the latter propagate more zonally and are generally meridionally trapped by midlatitude waveguides. Figure S9 clarifies the different character of these scales, showing the climatological stationary wave as a function of zonal wavenumber in MiMA, following Fig. 4c of Simpson et al. (2016).

a. *The intermediate-scale (zonal wavenumbers 4–7) stationary wave response*

According to the linear theory of barotropic Rossby waves in a zonal flow (Hoskins and Karoly 1981; Hoskins and Ambrizzi 1993), the background flow influences stationary waves through the total wavenumber K_s, which can be written as

$$K_s = (k^2 + l^2)^{1/2} = \left(\frac{\beta - \overline{u}_{yy}}{\overline{u}}\right)^{1/2}, \tag{3}$$

where k is the zonal wavenumber, l is the meridional wavenumber, β is the meridional gradient of planetary vorticity, and $\overline{u}$ is the time-mean zonal wind [Eq. (2.4) and (2.7) of Hoskins and Ambrizzi 1993]. Strengthened upper-tropospheric $\overline{u}$ (a response to strengthened mid- and upper-tropospheric meridional temperature gradients driven by increased CO_2) reduces K_s. Stationary waves adapt by reducing the zonal wavenumber k, inducing the lengthening of intermediate-scale waves, as waves 4 and 5 are preferred, while waves 6 and 7 are weakened (Simpson et al. 2016). This mechanism was applied to the Pacific–North American sector by Simpson et al. (2016), and we assess its relevance to the Euro-Atlantic sector.

Figure 3 shows the stationary wave of zonal wavenumbers 4–7 at 230 hPa. The wave lengthens in response to warming in some regions yet not in others. On the northern flank of the Mediterranean Sea (~40°–60°N), the $4xCO_2$ wave is in opposite phase to the $1xCO_2$ wave, likely significantly elongated by half a wavelength. However, to the south, over North Africa and the Arabian Peninsula, the length scale remains the same and only the amplitude strengthens. Overall, a strong positive anomaly is generated over the Mediterranean, stretching north over central Europe, similar in location to the full wave response (Fig. 2a), albeit weaker.

Over North America, the first-order response resembles an equatorward shift. A zonal lengthening and strengthening is found between ~20° and 40°N, propagating across the Atlantic Ocean, while further north over North America, the wave weakens significantly with no lengthening. Over East Asia and the northwest Pacific, the main response is a weakening of the wave, with slight lengthening.

We next decompose the intermediate-scale stationary wave into its three building blocks (Figs. 3b–d). The LSC-forced wave exhibits a general downstream lengthening and weakening, with a greater change in the Euro-Atlantic nodes. The OHT-forced wave generally strengthens between 20° and 40°N with no notable zonal change, while between 40° and 60°N, the $4xCO_2$ wave is of opposite phase to the $1xCO_2$ wave, especially in the Atlantic sector, similar to the full response in Fig. 3a. In East Asia and the west Pacific, the main response is a weakening of the wave. The orography-forced intermediate-scale wave shifts upstream and equatorward on the lee side of the Rocky Mountains and across the Atlantic, resulting in a positive anomaly over the Mediterranean. No change in the length scale is found downstream of the Himalaya and Tibetan Plateau and across the western and central Pacific. The wave weakens throughout the majority of the extratropics.

The lengthening response of intermediate-scale waves (Simpson et al. 2016) is not spatially uniform and while apparent in the LSC- and OHT-forced wave does not manifest in the orography-forced wave. A potential explanation lies in

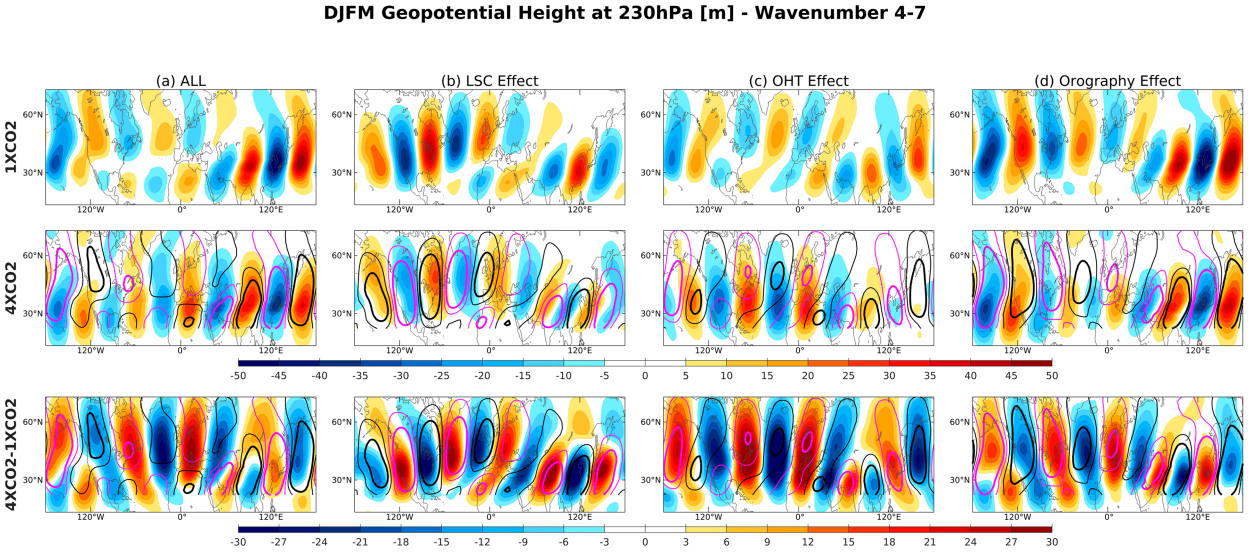

FIG. 3. As in Fig. 2, but for wavenumbers 4–7. The contours indicate the geopotential height of ±5 and ±15 m in 1xCO2 climatology.

the mechanical forcing of orography versus the thermal forcing of LSC and OHT, and the opposite response of the two to altered low-level zonal wind (Held and Ting 1990), as discussed in section 6c. The Mediterranean pressure anomaly in response to warming in the intermediate-scale waves (Fig. 3a) is a nonlinear response of the regional signature of these separate components and accounts for approximately 35% of the full response over the Mediterranean (Fig. 2a). This suggests further mechanism(s) is involved in the projected Mediterranean drying and stationary wave change over the Euro-Atlantic sector.

b. *The large-scale stationary wave response to warming*

We next assess the change in large-scale stationary waves with zonal wavenumbers 1–3, separating wavenumbers 1 and 2 from wavenumber 3 due to key differences between them. Figure 4 shows the change in zonal wavenumbers 1 and 2. The ridge over Europe, in both the present and future climate, is primarily associated with these wavenumbers (note the difference in the color scale with Fig. 3). As the climate warms, essentially all nodes strengthen in midlatitudes, while in the subtropics over Africa/Asia, the wave weakens (Fig. 4a), consistent with CMIP5 model-mean response in RCP8.5 (Wills et al. 2019). The Euro-Atlantic Ridge strengthens and expands, resulting in a positive anticyclonic anomaly over the Mediterranean Sea, Europe, and North Africa. The Hudson Bay low also strengthens and expands into the North Atlantic. This strengthening in response to $4xCO_2$ is the clearest in the two Atlantic sector nodes, suggesting a regional mechanism.

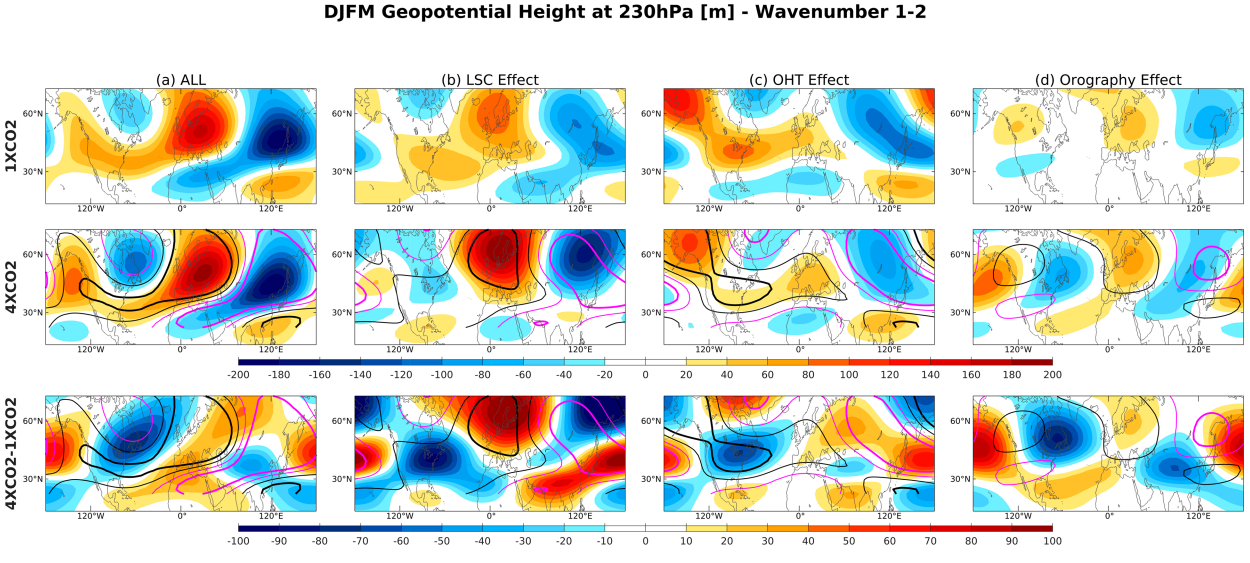

FIG. 4. As in Fig. 2, but for wavenumbers 1 and 2. The contours indicate the geopotential height of ±20 and ±60 m in 1xCO2 climatology.

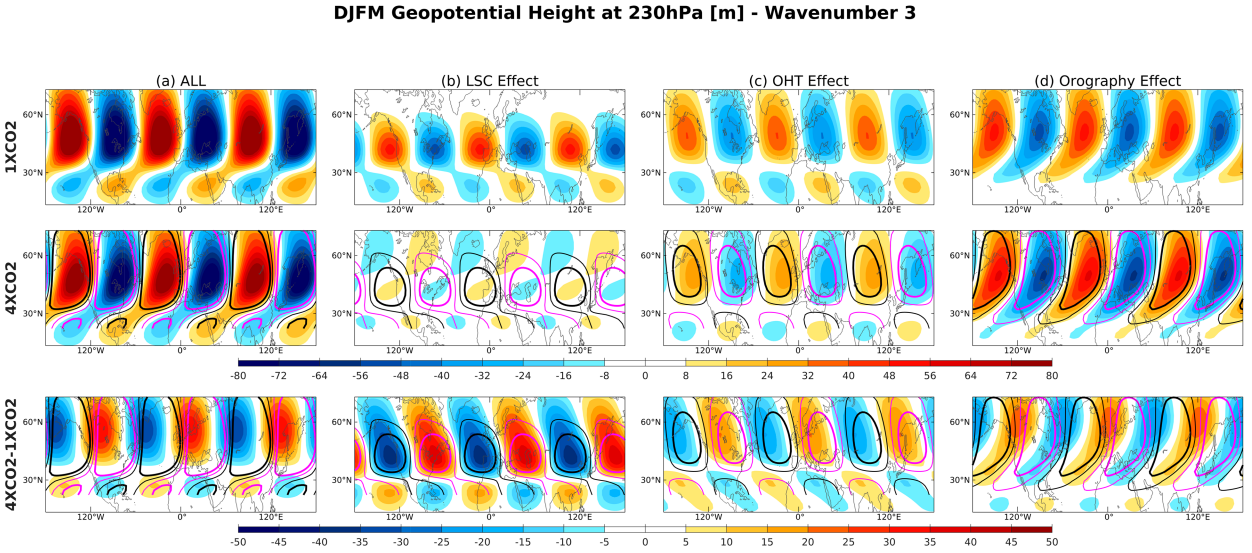

FIG. 5. As in Fig. 2, but for wavenumber 3. The contours indicate the geopotential height of ±8 and ±24 m in 1xCO2 climatology.

When decomposing the response into the stationary wave drivers (Figs. 4b–d), we find that the northern European anomaly is primarily due to the changes in the LSC-driven wave, while the OHT-driven wave forces a large part of the anomaly over central and eastern Europe and the Mediterranean Sea. Orography has a smaller but nonnegligible contribution. As in the full-spectrum wave, the sum of the changes from each of the building blocks does not even qualitatively resemble the total change in ALL.

The stationary wave of zonal wavenumber 3 propagates both zonally and meridionally (Fig. 5a). As the climate warms, the wave shifts downstream in phase, chiefly zonally, but also meridionally, and largely retains its amplitude. In 1xCO_2, the amplitude and spatial pattern of wave 3 in the midlatitudes are dominated by the influence of orography. As the climate warms, the orography-forced wave strengthens slightly and shifts downstream in the zonal direction, similar to the total response. The OHT-driven wave weakens and shifts downstream as well, and the LSC-driven wave weakens considerably, with no zonal shift. The weakening of the LSC-driven wave is consistent with reduced land–sea contrast in a warmer world. The response of wave 3 to warming is unique for each driver, with the overall response a nonlinear superposition of the three, amounting to 35%–40% of the positive anomaly to the north of the Mediterranean Sea in Fig. 2.

To explain the downstream shift of wave 3, we consider the horizontal group velocities of stationary Rossby waves [Eq. (2) of Simpson et al. 2016]:

$$c_{g,x} = \frac{2\overline{u}k^2}{k^2 + l^2} \quad \text{and} \quad c_{g,y} = \frac{2\overline{u}kl}{k^2 + l^2}, \tag{4}$$

where $\overline{u}$ is the zonal-mean zonal wind, k is the zonal wavenumber, and l is the meridional wavenumber. Increased $\overline{u}$ can result in a larger zonal group velocity so that wave activity can travel further east of the source before it is dissipated. This is consistent with the phase shift in both the zonal and meridional directions of wave 3 in response to warming. The results are similar if we consider the Rossby wave phase speed rather than the group velocity. While the nonlinearity of the problem does not allow a full physical interpretation of this response, the phase shift of wave 3 contributes significantly to the anomalous ridge over the Mediterranean in response to warming, especially on the northern flank.

The mechanisms and forcings governing the stationary wave response to warming vary across the zonal wavenumber spectrum. Waves 4–7 elongate downstream due to an altered stationary wavenumber, while wave 3 shifts downstream in phase, possibly due to enhanced group velocity. Waves 1 and 2 strengthen and expand in the Atlantic sector, likely due to the changes in surface forcing, as examined in the following section.

c. *Changes in the stationary wave surface forcing upstream of the Mediterranean Ridge*

We next utilize the zonally anomalous, steady-state thermodynamic balance [Eq. (2)] to understand how altered low-level temperature gradients and wind velocities translate to stationary wave changes over the Mediterranean. We first examine the changes in the temperature field in 4xCO_2 (Fig. 6), as these are the foundation for explaining the stationary wave changes using the thermodynamic budget. The two main zonally anomalous features in response to warming in the NH midlatitude Atlantic sector are enhanced warming over land compared to sea, expected as the climate warms (Sutton et al. 2007), and the NAWH. The two adjacent features generate a large zonal temperature gradient anomaly upstream of the Mediterranean (Fig. 6a). In our model, enhanced land warming and the NAWH are tied to the LSC and OHT building blocks, respectively. That is, when no LSC is present, the zonal temperature contrast between Europe and the central Atlantic disappears in 4xCO_2 (Fig. 6c) and so the enhanced

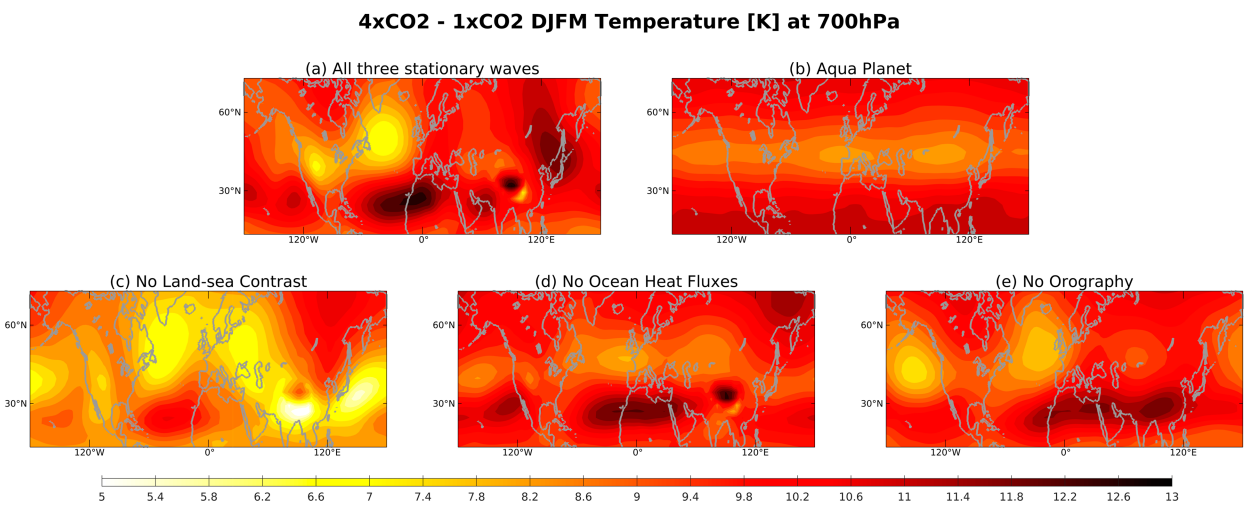

FIG. 6. DJFM $4xCO_2$–$1xCO_2$ temperature change (K) at 700 hPa for (a) ALL; (b) aquaplanet configuration with none of the building blocks; (c) no LSC, orography and OHT only; (d) no OHT, orography, and LSC only; (e) no orography, LSC, and OHT only.

land warming when LSC is turned on allows for a sharper zonal temperature gradient to develop. When OHT fluxes are not included, no NAWH forms in $4xCO_2$ (Fig. 6d) and so a prerequisite for the NAWH is the existence of OHT. The interaction between the NAWH and stationary waves upstream and downstream, and the formation of a NAWH in our model, despite the lack of a dynamical ocean, is discussed in section 6b.

Figure 7 shows the zonally anomalous steady-state thermodynamic balance [Eq. (2)] for ALL at 700 hPa. (For changes in the temperature field at 230 hPa for experiments 1–4, see Fig. S10.) The budget is essentially closed, with negligible residual (see Fig. S11). In $1xCO_2$, all terms in the budget contribute, but the leading order balance is between the zonal and meridional advection terms. The vertical term is important near topographic features, with significant cooling (heating) upslope (downslope) of large mountain ranges (Fig. 7c). The diabatic heating term exhibits a land/sea dipole pattern, in line with the winter land–sea temperature contrast. The transient eddy heat fluxes are downstream of the zonal advection anomalies (Figs. 7b,d).

As the climate warms, a large, cold zonal advection anomaly forms in the eastern North Atlantic, spreading inland along the European Atlantic coast (Fig. 7b, bottom). A warm zonal advection anomaly forms downstream over eastern Europe, with narrower zonal but similar meridional extent. These anomalies are chiefly balanced by the meridional advection in response to warming, which is of opposite sign to the zonal advection (Fig. 7a, bottom). The meridional heat advection anomalies are consistent with the location of the

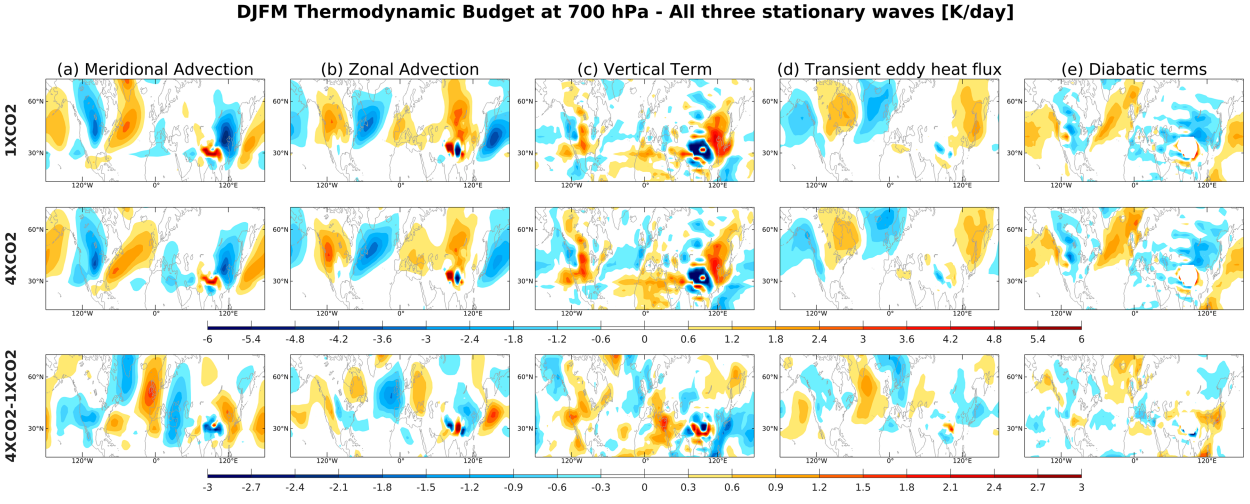

FIG. 7. DJFM zonally anomalous steady-state thermodynamic budget [Eq. (1)] at 700 hPa for ALL, displaying (a) meridional advection; (b) zonal advection; (c) vertical term; (d) heat fluxes by transient eddies; (e) diabatic heating due to latent heat release, radiation, and other nonconservative processes. The results from the (top) $1xCO_2$ and (middle) $4xCO_2$ integrations, and (bottom) their difference.

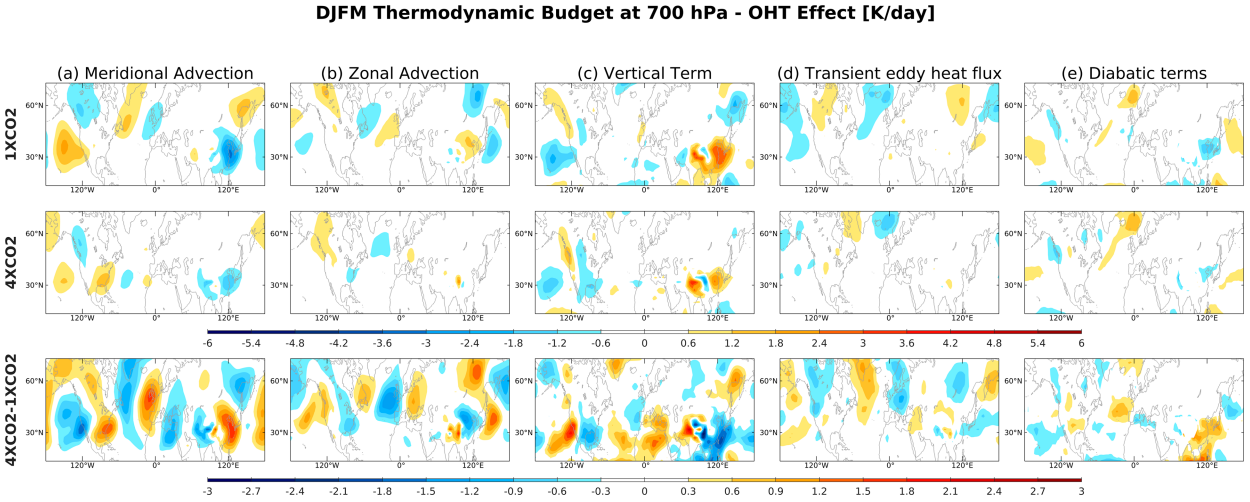

FIG. 8. As in Fig. 7 but for ALL–no OHT, isolating the OHT effect.

geopotential height anomaly in Fig. 2a. Warm vertical advection anomalies can be seen in the eastern Mediterranean (Fig. 7c, bottom), partially balancing the temperature change brought about by meridional northerly advection. Transient eddy heat fluxes also play an important role in the response to warming, with negative (positive) anomalies downstream (upstream) and poleward of the cold zonal advection anomaly in the North Atlantic, transmitting the anomaly upward in the vertical. In the upper troposphere, the transient eddy anomaly above the North Atlantic weakens and the balance between the zonal and meridional advection terms dominates (see Fig. S12).

The zonally anomalous thermodynamic budget detects the balance between zonal meridional advection changes in $4xCO_2$, yet it cannot establish causality, i.e., determine which term changes first and which subsequently responds. All the terms must balance each other by construction, and hence, one term cannot "force" any others. To tackle this difficulty, we compare the budget for ALL (Fig. 7) with that of the LSC- and OHT-driven stationary waves, as changes in both alter the zonal temperature gradient in the North Atlantic (Fig. 6) and can therefore establish causality. The NAWH, which forms in $4xCO_2$ only when OHT is activated, cools the lower-troposphere north and downstream of the cold SSTs, via a weakening of turbulent fluxes from the ocean to the atmosphere (Gervais et al. 2019). The relative cooling of the ocean compared to land as the climate warms (Sutton et al. 2007) weakens the low-level winter zonal temperature gradient and therefore reduces the warm zonal advection from the Atlantic Ocean into Europe.

The cold zonal advection anomaly over the eastern North Atlantic and European Atlantic coast in ALL (Fig. 7b) stems from a combination of LSC and OHT. The western and major part of the cold zonal advection anomaly, in the central and eastern North Atlantic, is caused by the changes in the OHT-forced wave (Fig. 8b). The eastern part of the cold anomaly, along the Atlantic coast and inland into Europe, is caused by altered LSC (Fig. 9b). For both LSC and OHT, the zonal advection term over the Euro-Atlantic is mostly balanced by the meridional advection term (Figs. 8a and 9a).

The zonal advection anomaly in response to warming in our experiments can be further decomposed as

$$\Delta\left(\overline{u}\frac{\partial\overline{\theta}}{\partial x}\right) \approx \Delta\overline{u}\frac{\partial\overline{\theta}}{\partial x}_{1xCO2} + \overline{u}_{1xCO2}\Delta\frac{\partial\overline{\theta}}{\partial x}, \quad (5)$$

where Δ is the difference between $4xCO_2$ and $1xCO_2$. This isolates the relative contribution of changes in the time-mean zonal wind $\overline{u}$ and the zonal temperature gradient $\partial\overline{\theta}/\partial x$ for the cold zonal advection anomaly in the eastern North Atlantic and along the European Atlantic coast. In this decomposition, we neglect the "Δ–Δ" term; nonetheless, the approximation holds well, with only a small residual. An altered zonal temperature gradient $\partial\overline{\theta}/\partial x$ in response to warming generates a cold zonal advection anomaly over the northeast Atlantic and western Europe (Fig. 10b), similar in amplitude to the zonal advection anomaly (Fig. 7b) and slightly larger in zonal extent. In contrast, the influence of the accelerated $\overline{u}$ in the absence of an altered zonal temperature gradient would be to further warm the Euro-Atlantic coast and western Europe (Fig. 10a), contrary to the advection anomaly.

We deduce that the cause of the large cold zonal advection anomaly in the North Atlantic in response to warming (Fig. 7b) is the altered zonal temperature gradient $\partial\overline{\theta}/\partial x$, not $\overline{u}$. A similar decomposition of the meridional advection response to warming shows that the anomaly is dominated by the changes in $\overline{v}$ as opposed to $\partial\overline{\theta}/\partial y$ (see Fig. S14). The net effect is that the changes in the zonal temperature gradient $\partial\overline{\theta}/\partial x$ in the northeast Atlantic, associated with the NAWH and with a weaker temperature gradient between Europe and the North Atlantic Ocean, force changes in the meridional wind and therefore a stationary wave change downstream over the Mediterranean.

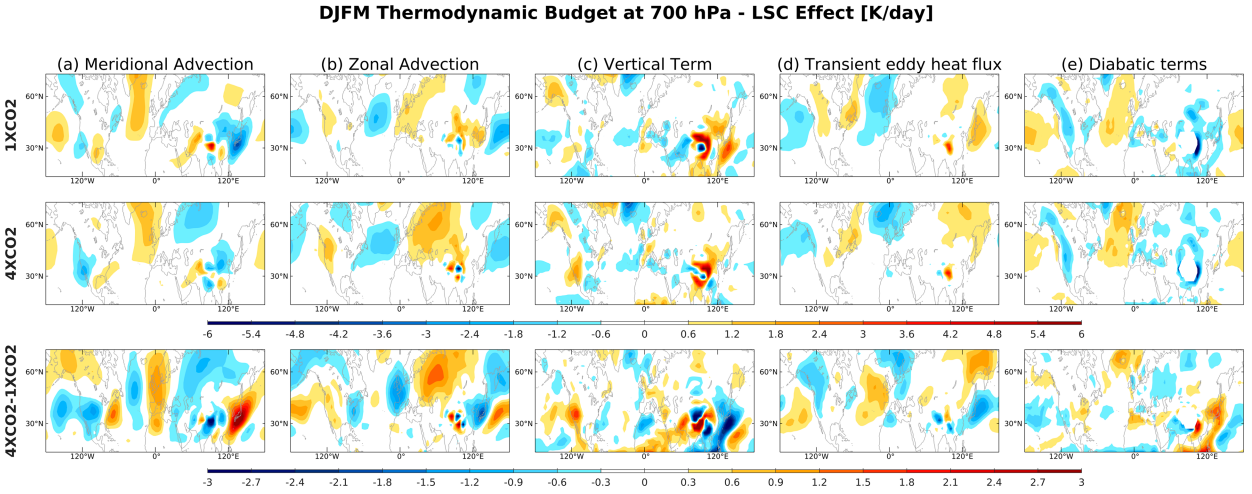

FIG. 9. As in Fig. 7 but for ALL–no LSC, isolating the LSC effect.

d. Relative Mediterranean cooling and regional land–sea contrast components

LSC changes play an important role in projected Mediterranean drying and the associated ridge (Figs. 1c and 2b). In this section, we examine which specific continent and/or body of water is most responsible. Motivated by the results of Tuel and Eltahir (2020, see section 2), we first consider the role of the Mediterranean Sea. Specifically, we manipulate the land-mask such that the Mediterranean Sea is changed into land, leaving everything else the same (Fig. 11b; experiment 5 in Table 1, "no Mediterranean Sea"). The difference in the stationary wave response to 4xCO_2 between ALL and no Mediterranean Sea is shown in Fig. 12b. A ridge develops over the region due to the Mediterranean LSC changes (Fig. 12b), but with a significantly smaller spatial extent and weaker amplitude, relative to ALL (Fig. 2a) and to the full LSC effect (Fig. 12a). Moreover, we find an enhanced decrease in precipitation in no Mediterranean Sea compared to ALL (Fig. 1f). Hence, the mechanism of Tuel and Eltahir (2020) plays a minor role at most in our experiments.

We next isolate the role of the northeast Atlantic LSC by changing Europe and North Africa to sea (Fig. 11c; experiment 6 in Table 1). The stationary wave response to the altered Atlantic coast gradient (Fig. 12c) is much larger compared to that of the Mediterranean gradient (Fig. 12b) and qualitatively captures the full LSC effect (Fig. 12a), albeit weaker. A similar change in precipitation is found as well (cf. Figs. 1c,g), suggesting that in terms of regional LSC components, it is the altered North Atlantic coastal gradient, not the Mediterranean gradient, which most influences the projected large-scale circulation changes (i.e., the upper-level ridge) and the consequent Mediterranean drying.

Further experiments, isolating the role of the NH continents within the LSC-forced stationary wave, show that the LSC forcing in 4xCO_2 is dominated by enhanced warming of Eurasia (Fig. 12d), in line with previous studies (e.g., Portal et al. 2022). This point is further apparent when examining the low-level stationary wave (Figs. S7 and S8). Some extrema of the LSC effect, such as the positive anomalies in the polar North Atlantic and in the North Pacific Ocean, are governed by the relative warming of North America (Fig. 12e). However, these anomalies are generally overpowered by changes forced by the other stationary wave building blocks and are far weaker in ALL (Fig. 2a) compared to the forcing exerted by LSC alone (Fig. 2b). Further reasoning of the continental forcing of stationary wave changes is beyond the scope of this paper.

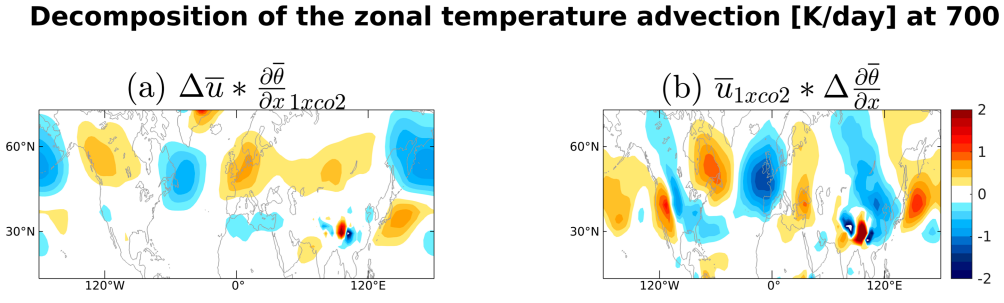

FIG. 10. 4xCO_2–1xCO_2 zonal advection term decomposed into (a) the forcing exerted by the change in zonal-mean zonal wind and (b) the forcing exerted by the change in the zonal temperature gradient, as in Eq. (5). The term Δ denotes the difference between 4xCO_2 and 1xCO_2.

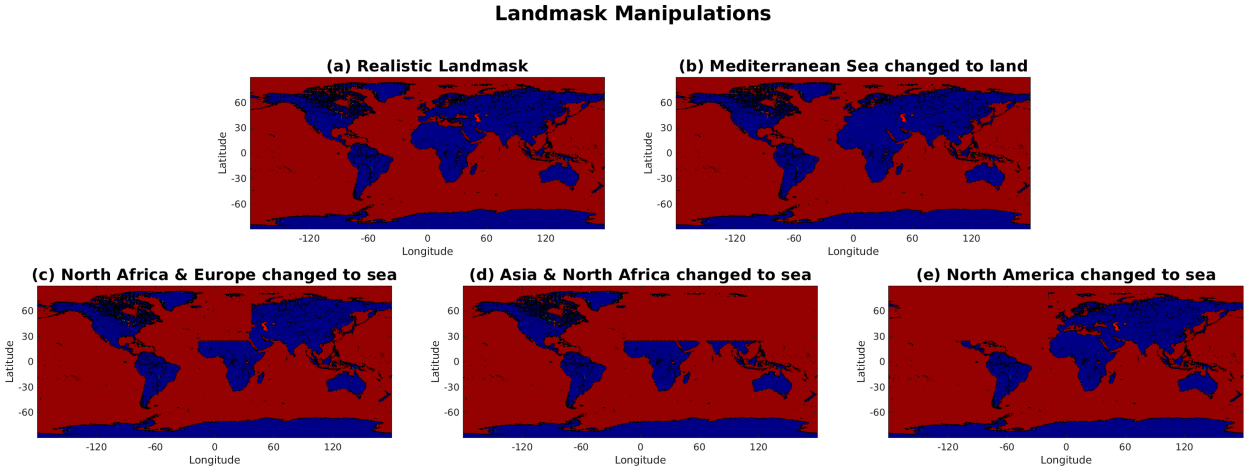

FIG. 11. Landmask manipulation for experiments 5–8 in Table 1: (a) Realistic landmask; (b) Mediterranean Sea changed to land; (c) Europe and North Africa changed to sea; (d) Eurasia changed to sea; (e) North America changed to sea.

6. Discussion

The three building blocks which ultimately force atmospheric stationary waves each exhibit unique responses to warming and contribute differently to Mediterranean drying. Changes in the LSC-driven stationary waves act to significantly alter the location, amplitude, and meridional extent of the Mediterranean Ridge, but are not its underlying cause. Changes in OHT-forced stationary waves have a direct effect on the Mediterranean Ridge, via the downstream response to the NAWH. Changes in the orography-forced wave are governed by the changes in the low-level wind and contribute to Mediterranean drying via an indirect downstream effect of modified wave propagation from large-scale topography. These three interact nonadditively such that one cannot quantify the precise contribution of each to Mediterranean drying. While the nonlinearity of the building blocks does not allow a simple decomposition, we have identified three key mechanistic pathways that matter quantitatively, and when combined, they drive the stationary wave response over the Mediterranean. Two have appeared in some form in the literature, though typically not in the context of Mediterranean drying. We next discuss further details and reasoning of the mechanisms, and their regional manifestations.

a. *The lengthening response of intermediate-scale stationary waves*

The lengthening response to warming in intermediate-scale stationary waves (Simpson et al. 2016) varies both zonally and

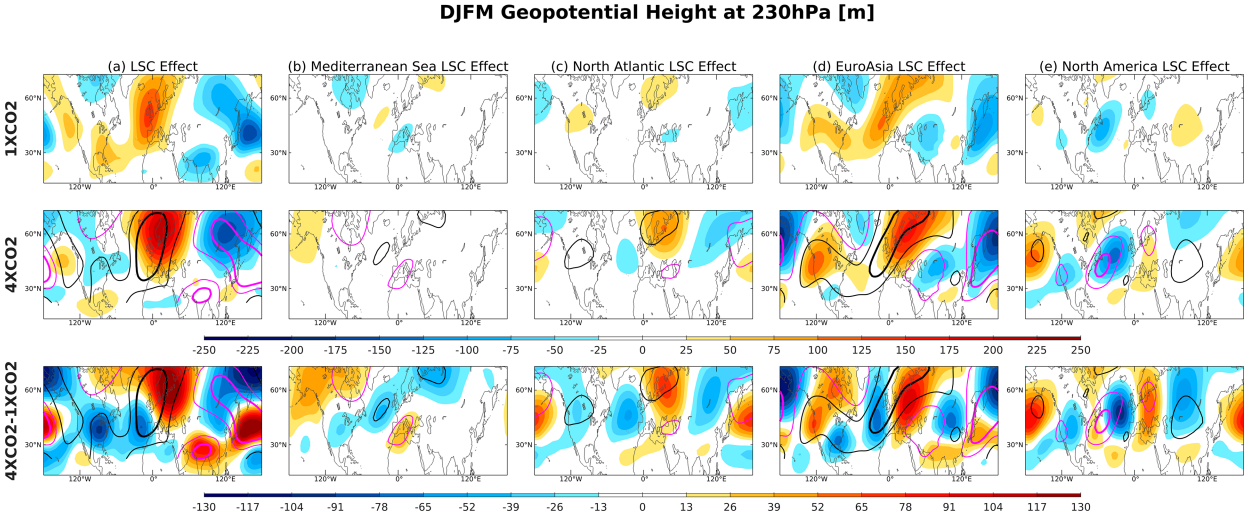

FIG. 12. As in Fig. 2, but for (a) ALL–no LSC, isolating the LSC effect (repeated from Fig. 2b); (b) ALL–"Mediterranean Sea changed to land," isolating the Mediterranean LSC effect; (c) ALL–"Europe and North Africa changed to sea," isolating the Euro-Atlantic LSC effect; (d) ALL–"Eurasia changed to sea," isolating the Eurasia LSC effect; (e) ALL–"North America changed to sea," isolating the North America LSC effect.

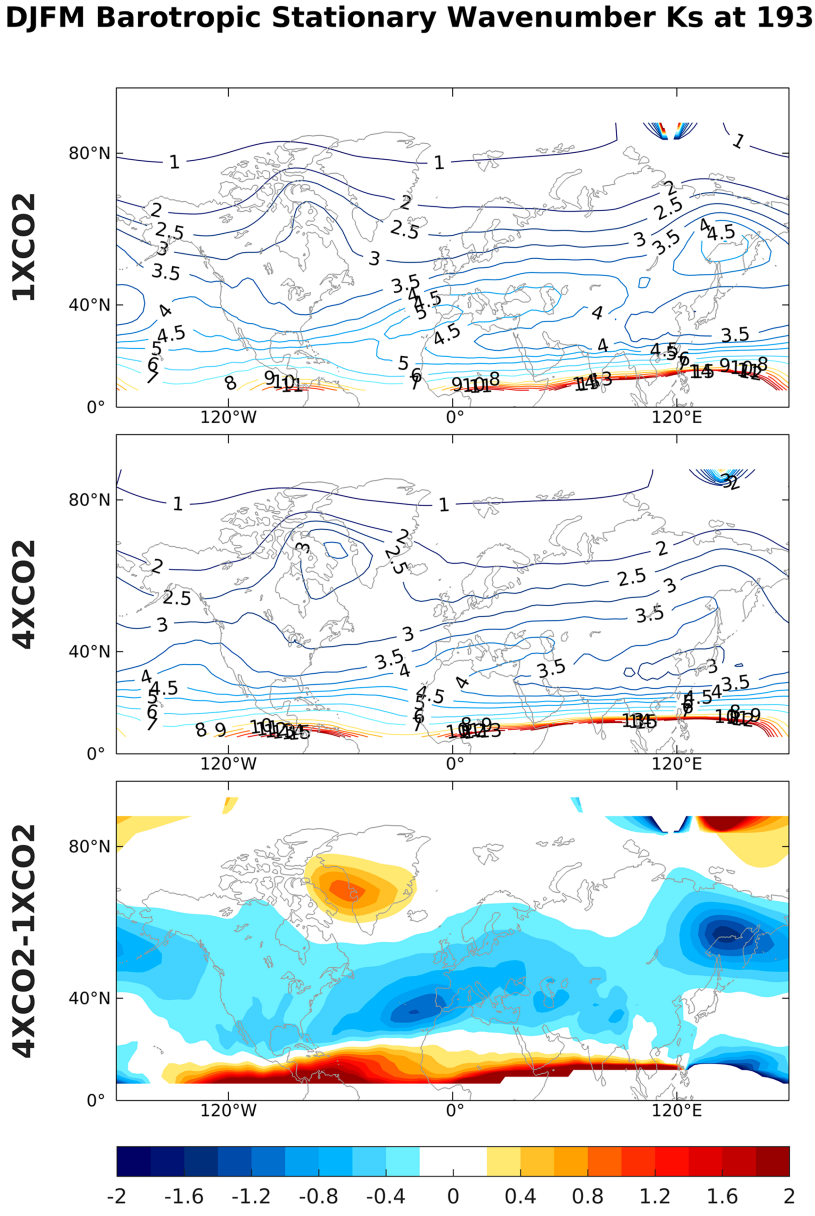

FIG. 13. Barotropic stationary wavenumber K_s at 193 hPa in ALL, for 1xCO_2, 4xCO_2, and 4xCO_2–1XCO_2. Contours are [0:1:2, 2.5:0.5:4.5, 6:1:15].

meridionally (Fig. 3; section 5a). The spatial variance can be understood by looking at the climatological barotropic stationary wavenumber K_s (Fig. 13). We find a good match between areas of large regional and upstream decrease in K_s in Fig. 13a and areas of significant downstream lengthening of the stationary wave in Fig. 3a. In particular, there is a large decrease in K_s both directly over and upstream of the Mediterranean Sea and western Europe, but not for North Africa. The wavenumber 4–7 stationary wave lengthens accordingly, with no shift over North Africa and the Arabian Peninsula and a large shift over Europe and the Mediterranean. Over North America, we see a larger decrease in K_s between 20° and 40°N and less between 40° and 60°N, and the lengthening follows accordingly. A similar match is found over East Asia and the northwest Pacific. This reasoning, following Simpson et al. (2016), is further clarified by the spatial variance in the upper-level zonal-wind change (Fig. S15), which directly influences K_s [Eq. (3)]. A deviation from this theoretical reasoning is found over central Asia, where a strengthening of the upper-level zonal wind does not cause a significant lengthening of the wave. The vicinity to large orography may dominate the response in this region (see section 6c).

b. *The North Atlantic warming hole and LSC*

The response of the winter zonal wavenumber 1–2 stationary waves over the North Atlantic and Europe strongly

resembles the midtropospheric geopotential height response downstream to an enhanced winter NAWH, as isolated by Gervais et al. (2019). In particular, compare Fig. 4a with Figs. 3 and 5 of Gervais et al. (2019). This is further demonstrated when comparing $4xCO_2$–$1xCO_2$ v^* at 230 hPa in our model with the response to an enhanced NAWH of the dynamic tropopause wind speed; compare Fig. S3a showing the wave 1–2 v^* with Fig. 3 of Gervais et al. (2019). This response coincides with equivalent barotropic elongation and strengthening of the North Atlantic jet (Fig. 14; Fig. S15) in agreement with CMIP5 multimodel mean projections in RCP8.5 (Simpson et al. 2014), which consistent with geostrophic balance translates to increased geopotential height equatorward of the jet, over the Mediterranean and Europe.

The thermodynamic budget illustrates, from a stationary wave perspective, the mechanism by which the NAWH generates a high pressure anomaly downstream over the Mediterranean in future projections (section 5c; Fig. 8), complementary to that shown in Gervais et al. (2019). The thermodynamic budget additionally shows that reduced warming of the North Atlantic Ocean relative to Eurasia further enhances the downstream response to the NAWH (Fig. 9). The Euro-Atlantic meridional advection anomalies in the OHT-forced wave (Fig. 8a) have a similar amplitude to ALL (Fig. 7a), while those of the LSC-forced wave are weaker and meridionally elongated. We conclude that the NAWH, associated with the OHT-driven wave in our model, contributes directly to the rain-suppressing Mediterranean Ridge, while the altered LSC impacts the pressure field over a larger spatial extent, and affects the Mediterranean Ridge indirectly. These changes are most apparent in wavenumbers 1–2.

Delworth et al. (2022) found that while climate change mitigation can reduce summer drying in the Mediterranean, winter drying continues. This is attributed to a GHG-induced weakening of the Atlantic meridional overturning circulation (AMOC), which persists for decades after reduction in CO_2 emissions, and affects the Mediterranean via cooling in the subpolar North Atlantic. An altered AMOC cannot be linked to the results in our model, as we do not have a dynamical ocean. However, a NAWH appears in our model despite the lack of a dynamical ocean (Fig. 6a). This non-AMOC-driven NAWH has been previously found by He et al. (2022), who show that 90% of the subpolar North Atlantic cooling relative to the global ocean temperature arises from atmospheric processes and not ocean dynamics. The NAWH in their study results from increased north-westerlies upstream in the subpolar North Atlantic in response to warming, that increase heat loss from the ocean surface through enhanced air–sea temperature differences and turbulent heat fluxes. This can be seen in our model as well (Figs. 7a,b and 10a and Fig. S14a). The atmospheric-born NAWH found by He et al. (2022) and in our model, along with the downstream circulation response, challenges the importance of AMOC weakening for future Mediterranean drying and, consequently, the hindered reversibility of winter drying (Delworth et al. 2022).

One might wonder why a NAWH appears in the $4xCO_2$ experiments only when OHT is activated. OHT is constant in our model, and atmospheric-born cooling of the subpolar North Atlantic relies on other circulation responses to warming (He et al. 2022; Fig. 7). This may be because the subpolar cooling is only significantly felt in the presence of western boundary currents, particularly the Gulf Stream (Kaspi and Schneider 2011). Either way, the thermodynamic budget directly links the NAWH to the ridge response over the Mediterranean, and isolating the various mechanisms that lead to the NAWH is beyond the scope of this work.

The sensitivity of the low-level circulation over the Mediterranean to changes in the upper-level stationary wave pattern has been related by Tuel et al. (2021b) to a relatively weak vertical shear of zonal winds in the region. They further attribute the seasonality of the projected Mediterranean anticyclonic circulation to seasonal variations in low-level static stability, that enable surface SST changes to propagate upward more efficiently in the winter and prevent this propagation during summer. They focus on the reduced Mediterranean temperature gradient (Tuel and Eltahir 2020), which we found to be negligible in our model (section 5d); however, this reasoning holds for circulation changes forced by other regional temperature anomalies as well.

c. *The role of orographic stationary waves in Mediterranean drying*

While the two thermally driven stationary waves in our model show a clear and largely explainable contribution to Mediterranean drying, the role of the orographically driven wave is more complex. The orographically forced wave above and downstream of the Himalayas and the Tibetan Plateau weakens in $4xCO_2$, yet above and downstream of the Rocky Mountains, the wave strengthens and elongates (Fig. 2). The latter contributes to the ridge over the Mediterranean and western Europe.

The stationary wave forced by orography is of smaller zonal wavelength relative to the thermally forced ones, both in our model (Fig. 2) and in studies using a steady-state model (Held et al. 2002). Orography plays a smaller role in $1xCO_2$ waves 1–2 relative to the other building blocks (Fig. 4) and is more important for wavenumbers 3–7. The amplitude and spatial pattern of wave 3 are dominated by the influence of orography, both in $1xCO_2$ and in response to warming (Fig. 5). The main response of orographic wave 3 in $4xCO_2$ is a downstream phase shift, similar to the total wave-3 response (Figs. 5a,d). This may be due to the increased group velocity in response to enhanced $\overline{u}$, yet it remains unclear why this mechanism is found only in wave 3.

The lengthening mechanism of intermediate-scale stationary waves (Simpson et al. 2016) is not apparent in orographic waves. Instead, the wave generally weakens in $4xCO_2$ (Fig. 3d), in agreement with Wills and Schneider (2018). This response is related to the changes in the zonal wind. The amplitude of orographically forced stationary waves is proportional to the velocity of wind impinging on the orography (Held and Ting 1990; Wills and Schneider 2018). Upstream of the Rocky Mountains, the low-level jet shifts poleward in our model, resulting in weaker westerly winds impinging on the mountain range (Fig. 14). Accordingly, the most pronounced weakening in the orographically

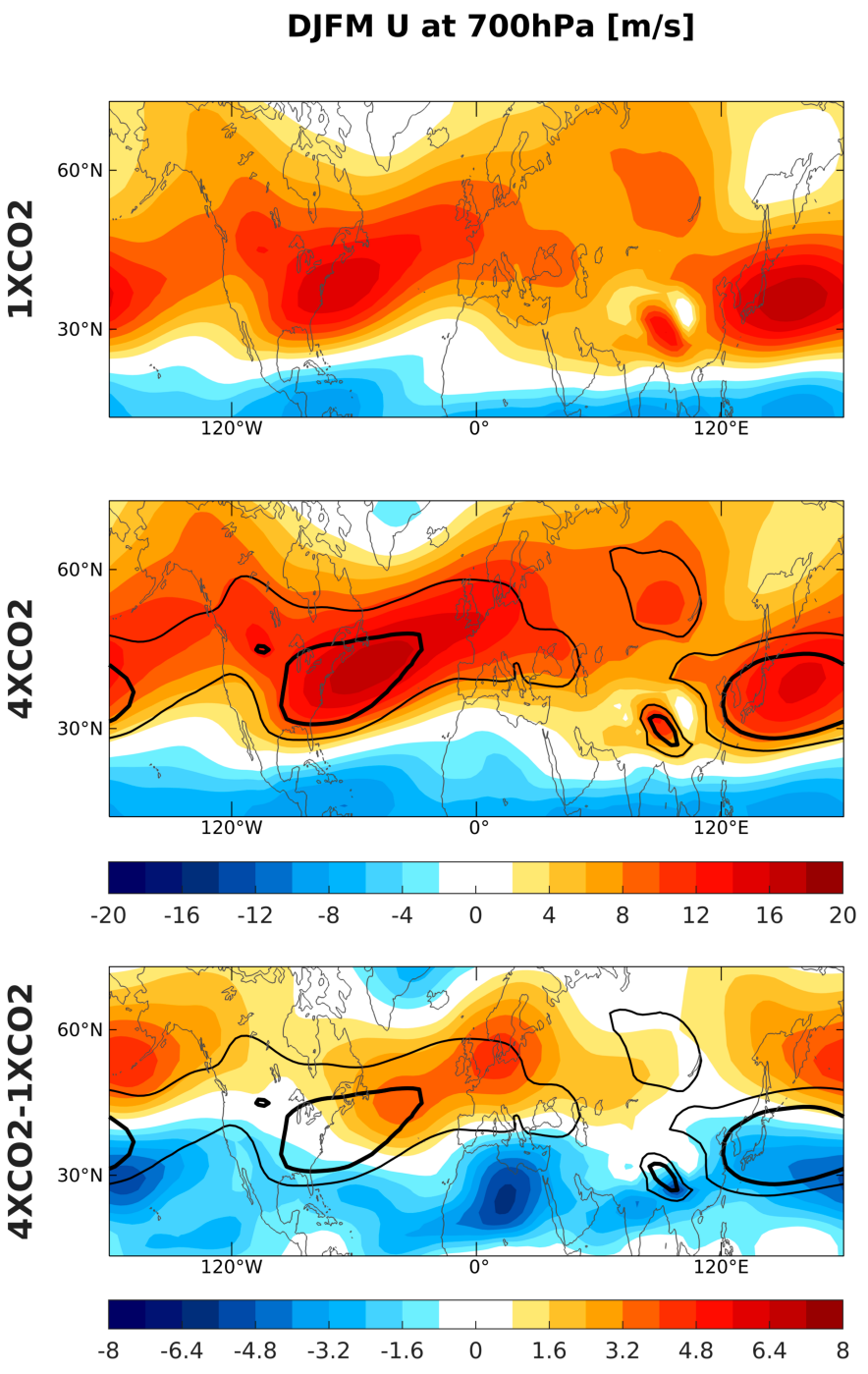

FIG. 14. Zonal-wind U at 700 hPa in ALL, for $1xCO_2$, $4xCO_2$, and $4xCO_2$–$1XCO_2$. Contours in (middle) and (bottom) mark the $1xCO_2$ climatology from (top), indicating the velocity of 8 and 12 m s^{-1} in $1xCO_2$ climatology.

forced intermediate-scale stationary waves is seen downstream of the Rocky Mountains (Fig. 3d), propagating until western Europe and reinforcing the northern part of the Mediterranean Ridge. Upstream of the Himalayas and the Tibetan Plateau, we see a more moderate weakening of the low-level winds (Fig. 14), consistent with the moderate weakening of the wave downstream (Fig. 3d). In areas further from orographic influence, such as southwest North America and North Africa, the wave strengthens.

Orographic wave 3 lies farther north than waves 4–7, centered poleward of the large-scale NH orography (Fig. 5). The poleward shift of low-level winds in a warmer climate

generally brings stronger winds to the northern midlatitudes, in our model (Fig. 14) and in CMIP5 models (Simpson et al. 2014; Wills et al. 2019). This may explain the strengthening of orography-forced wave 3, in contrast to the weakening of the LSC- and OHT-forced waves, as the amplitude of orographic waves is proportional to the speed of low-level winds, while thermally forced waves vary inversely (Held and Ting 1990). Future work should be done to better understand the response of the orographic-forced stationary wave to warming and in particular the phase change in the orography-dominated zonal wavenumber 3.

d. *The role of changes in synoptic-scale eddies*

One may ask whether the high pressure anomaly over the Mediterranean in response to warming is a result of changes in transient synoptic-scale variability rather than changes in stationary waves. To answer this question, we applied a 10-day low-pass filter to the geopotential height field ($Z230_{low}$) and then compute the response of the zonally asymmetric component of $Z230_{low}$ to $4XCO_2$ ($Z230^*_{low}$; Fig. S5a). The response of $Z230^*_{low}$ is very similar to using the unfiltered $Z230^*$ (Fig. 2a).

Yet, even with a low-pass filter of the geopotential height variability, there can be a stationary influence of changes in high-frequency fluxes on the stationary wave structure. To isolate this effect, one needs to quantify the high-frequency eddies directly. Figure 7d quantifies the effect of transient eddies as part of the thermodynamic budget, and in all cases (in $1xCO_2$, $4xCO_2$, and $4xCO_2$–$1xCO_2$), its effect is smaller than the stationary components. We conclude that the projected Mediterranean Ridge does not primarily result from the changes in synoptic-scale variability, although transient eddies do contribute to barotropizing the anomaly, as shown in section 5c.

We do not focus on regional boundary layer drivers and mesoscale features, as this is beyond the scope of this paper and the resolution of our model. These processes are indeed important for regional hydroclimatic changes, and it is conceivable they would contribute to the understanding of Mediterranean drying. This should be the subject of a complementary study.

7. Conclusions

Projected precipitation decline in the Mediterranean is closely tied to the changes in NH winter stationary waves in response to warming (section 4; Figs. 1 and 2). An anomalous, rain-suppressing ridge is projected to develop over the Mediterranean, caused by a combination of several mechanisms. We argue that the three principal mechanisms are as follows:

1) **Lengthening of intermediate-scale stationary waves** (sections 5a and 6a): Enhanced subtropical upper-tropospheric zonal wind elongates waves of zonal wavenumbers 4–7 (Fig. 3, following Simpson et al. 2016). This mechanism is apparent in stationary waves forced by land–sea contrast and ocean heat transport, yet does not manifest for orographic waves, and is most prominent in regions downstream of enhanced zonal wind. This effect is responsible for approximately 35% of the total ridging response over the Mediterranean.
2) **Downstream response to the North Atlantic warming hole and altered Atlantic land–sea contrast** (sections 5b,c and 6b): the North Atlantic warming hole alters the temperature gradient upstream of the Mediterranean and influences the circulation via increased baroclinicity (Gervais et al. 2019) and altered zonal temperature advection (Figs. 7 and 10). This response to warming is most apparent in the large-scale (zonal wavenumbers 1–2) stationary wave anomalies that form over the North Atlantic and western Europe, consistent with a strengthening of the North Atlantic eddy-driven jet and high pressure above the Mediterranean (Figs. 4a,c). Additional contribution to the wave 1–2 anomaly arises from enhanced warming of the Eurasian landmass relative to the Atlantic Ocean, which modifies the pressure field in the northeast Atlantic over a large spatial extent (Fig. 4b), and affects the Mediterranean Ridge indirectly. Approximately 30%–40% of the total ridge is associated with this mechanism.
3) **The planetary-scale orographic wave-3 response to warming** (sections 5b and 6c): A downstream phase shift of stationary wave 3 (Figs. 5a,d), possibly due to increased group velocity in response to enhanced low-level winds, which causes wave activity to travel further east of the source. This response is primarily associated with changes in the circulation response to orographic forcing and contributes ~35%–40% of the northwestern part of the projected Mediterranean Ridge. We are not aware of previous studies linking this mechanism to Mediterranean drying.

In our experiments, reduced warming of the Mediterranean Sea with respect to land (Tuel and Eltahir 2020) causes a weak anticyclonic circulation over the region in response to warming. Its contribution to the large-scale circulation changes and projected drying in the Mediterranean region, however, is much smaller than the three aforementioned effects (Fig. 1f; Fig. 12b in section 5d).

Our results highlight the nonlinear and nonadditive behavior of the zonally asymmetric circulation response to warming (Fig. 2; section 4). However, by decomposing this response according to wavenumber, we are able to quantitatively disentangle NH stationary wave changes, identify key mechanisms governing the change, and further clarify the role of large-scale circulation changes for the projected drying of the Mediterranean region. Ongoing work is examining whether intermodel spread of Mediterranean climate projections in CMIP models can be related to the mechanisms proposed in this study and thus better understand the uncertainty in projections of Mediterranean climate. The results of this work will be reported in a companion study.

Acknowledgments. B. K. and C. I. G. acknowledge the support of the Israel Science Foundation (Grant Agreement 1727/21). C. I. G. and E. P. G. are also supported by the U.S.–Israel Binational Science Foundation (BSF) Grant 2020316. E.P.G. acknowledges the support from the U.S. NSF through Grant OAC-2004572.

Data availability statement. The version of MiMA used in this study, including the modified source code, can be downloaded at https://github.com/ianpwhite/MiMA/releases/tag/MiMA-ThermalForcing-v1.0beta (with https://doi.org/10.5281/zenodo.4523199).

REFERENCES

Armon, M., F. Marra, Y. Enzel, D. Rostkier-Edelstein, C. I. Garfinkel, O. Adam, U. Dayan, and E. Morin, 2022: Reduced rainfall in future heavy precipitation events related to contracted rain area despite increased rain rate. *Earth's Future*, **10**, e2021EF002397, https://doi.org/10.1029/2021EF002397.

Brogli, R., S. L. Sørland, N. Kröner, and C. Schär, 2019: Causes of future Mediterranean precipitation decline depend on the season. *Environ. Res. Lett.*, **14**, 114017, https://doi.org/10.1088/1748-9326/ab4438.

Byrne, M. P., and P. A. O'Gorman, 2015: The response of precipitation minus evapotranspiration to climate warming: Why the "wet-get-wetter, dry-get-drier" scaling does not hold over land. *J. Climate*, **28**, 8078–8092, https://doi.org/10.1175/JCLI-D-15-0369.1.

Charney, J. G., and P. G. Drazin, 1961: Propagation of planetary-scale disturbances from the lower into the upper atmosphere. *J. Geophys. Res.*, **66**, 83–109, https://doi.org/10.1029/JZ066i001p00083.

Cos, J., F. Doblas-Reyes, M. Jury, R. Marcos, P.-A. Bretonnière, and M. Samsó, 2022: The Mediterranean climate change hotspot in the CMIP5 and CMIP6 projections. *Earth Syst. Dyn.*, **13**, 321–340, https://doi.org/10.5194/esd-13-321-2022.

Delworth, T. L., W. F. Cooke, V. Naik, D. Paynter, and L. Zhang, 2022: A weakened AMOC may prolong greenhouse gas–induced Mediterranean drying even with significant and rapid climate change mitigation. *Proc. Natl. Acad. Sci. USA*, **119**, e2116655119, https://doi.org/10.1073/pnas.2116655119.

Drijfhout, S., G. J. van Oldenborgh, and A. Cimatoribus, 2012: Is a decline of AMOC causing the warming hole above the North Atlantic in observed and modeled warming patterns? *J. Climate*, **25**, 8373–8379, https://doi.org/10.1175/JCLI-D-12-00490.1.

Elbaum, E., C. I. Garfinkel, O. Adam, E. Morin, D. Rostkier-Edelstein, and U. Dayan, 2022: Uncertainty in projected changes in precipitation minus evaporation: Dominant role of dynamic circulation changes and weak role for thermodynamic changes. *Geophys. Res. Lett.*, **49**, e2022GL097725, https://doi.org/10.1029/2022GL097725.

Freitas, A. C. V., and V. B. Rao, 2014: Global changes in propagation of stationary waves in a warming scenario. *Quart. J. Roy. Meteor. Soc.*, **140**, 364–383, https://doi.org/10.1002/qj.2151.

Frierson, D. M. W., I. M. Held, and P. Zurita-Gotor, 2006: A gray-radiation aquaplanet moist GCM. Part I: Static stability and eddy scale. *J. Atmos. Sci.*, **63**, 2548–2566, https://doi.org/10.1175/JAS3753.1.

Garfinkel, C. I., O. Adam, E. Morin, Y. Enzel, E. Elbaum, M. Bartov, D. Rostkier-Edelstein, and U. Dayan, 2020a: The role of zonally averaged climate change in contributing to intermodel spread in CMIP5 predicted local precipitation changes. *J. Climate*, **33**, 1141–1154, https://doi.org/10.1175/JCLI-D-19-0232.1.

——, I. White, E. P. Gerber, and M. Jucker, 2020b: The impact of SST biases in the tropical east Pacific and Agulhas Current region on atmospheric stationary waves in the Southern Hemisphere. *J. Climate*, **33**, 9351–9374, https://doi.org/10.1175/JCLI-D-20-0195.1.

——, ——, ——, ——, and M. Erez, 2020c: The building blocks of Northern Hemisphere wintertime stationary waves. *J. Climate*, **33**, 5611–5633, https://doi.org/10.1175/JCLI-D-19-0181.1.

——, B. Keller, O. Lachmy, I. White, E. P. Gerber, M. Jucker, and O. Adam, 2024: Impact of parameterized convection on the storm track and near-surface jet response to global warming: Implications for mechanisms of the future poleward shift. *J. Climate*, **37**, 2541–2564, https://doi.org/10.1175/JCLI-D-23-0105.1.

Gervais, M., J. Shaman, and Y. Kushnir, 2018: Mechanisms governing the development of the North Atlantic warming hole in the CESM-LE future climate simulations. *J. Climate*, **31**, 5927–5946, https://doi.org/10.1175/JCLI-D-17-0635.1.

——, ——, and ——, 2019: Impacts of the North Atlantic warming hole in future climate projections: Mean atmospheric circulation and the North Atlantic jet. *J. Climate*, **32**, 2673–2689, https://doi.org/10.1175/JCLI-D-18-0647.1.

Giorgi, F., 2006: Climate change hot-spots. *Geophys. Res. Lett.*, **33**, L08707, https://doi.org/10.1029/2006GL025734.

——, and P. Lionello, 2008: Climate change projections for the Mediterranean region. *Global Planet. Change*, **63**, 90–104, https://doi.org/10.1016/j.gloplacha.2007.09.005.

He, C., A. C. Clement, M. A. Cane, L. N. Murphy, J. M. Klavans, and T. M. Fenske, 2022: A North Atlantic warming hole without ocean circulation. *Geophys. Res. Lett.*, **49**, e2022GL100420, https://doi.org/10.1029/2022GL100420.

He, J., and B. J. Soden, 2017: A re-examination of the projected subtropical precipitation decline. *Nat. Climate Change*, **7**, 53–57, https://doi.org/10.1038/nclimate3157.

Held, I. M., 1983: Stationary and quasi-stationary eddies in the extratropical troposphere: Theory. *Large-Scale Dynamical Processes in the Atmosphere*, Academic Press, 127–168.

——, and M. Ting, 1990: Orographic versus thermal forcing of stationary waves: The importance of the mean low-level wind. *J. Atmos. Sci.*, **47**, 495–500, https://doi.org/10.1175/1520-0469(1990)047<0495:OVTFOS>2.0.CO;2.

——, and B. J. Soden, 2006: Robust responses of the hydrological cycle to global warming. *J. Climate*, **19**, 5686–5699, https://doi.org/10.1175/JCLI3990.1.

——, M. Ting, and H. Wang, 2002: Northern winter stationary waves: Theory and modeling. *J. Climate*, **15**, 2125–2144, https://doi.org/10.1175/1520-0442(2002)015<2125:NWSWTA>2.0.CO;2.

Hoskins, B. J., and D. J. Karoly, 1981: The steady linear response of a spherical atmosphere to thermal and orographic forcing. *J. Atmos. Sci.*, **38**, 1179–1196, https://doi.org/10.1175/1520-0469(1981)038<1179:TSLROA>2.0.CO;2.

——, and T. Ambrizzi, 1993: Rossby wave propagation on a realistic longitudinally varying flow. *J. Atmos. Sci.*, **50**, 1661–1671, https://doi.org/10.1175/1520-0469(1993)050<1661:RWPOAR>2.0.CO;2.

Iacono, M. J., J. S. Delamere, E. J. Mlawer, M. W. Shephard, S. A. Clough, and W. D. Collins, 2008: Radiative forcing by long-lived greenhouse gases: Calculations with the AER radiative transfer models. *J. Geophys. Res.*, **113**, D13103, https://doi.org/10.1029/2008JD009944.

Joseph, R., M. Ting, and P. J. Kushner, 2004: The global stationary wave response to climate change in a coupled GCM. *J. Climate*, **17**, 540–556, https://doi.org/10.1175/1520-0442(2004)017<0540:TGSWRT>2.0.CO;2.

Jucker, M., and E. P. Gerber, 2017: Untangling the annual cycle of the tropical tropopause layer with an idealized moist model. *J. Climate*, **30**, 7339–7358, https://doi.org/10.1175/JCLI-D-17-0127.1.

Kaspi, Y., and T. Schneider, 2011: Winter cold of eastern continental boundaries induced by warm ocean waters. *Nature*, **471**, 621–624, https://doi.org/10.1038/nature09924.

Lionello, P., and F. Giorgi, 2007: Winter precipitation and cyclones in the mediterranean region: Future climate scenarios in a regional simulation. *Adv. Geosci.*, **12**, 153–158, https://doi.org/10.5194/adgeo-12-153-2007.

Neelin, J. D., B. Langenbrunner, J. E. Meyerson, A. Hall, and N. Berg, 2013: California winter precipitation change under global warming in the Coupled Model Intercomparison Project phase 5 ensemble. *J. Climate*, **26**, 6238–6256, https://doi.org/10.1175/JCLI-D-12-00514.1.

Portal, A., C. Pasquero, F. D'Andrea, P. Davini, M. E. Hamouda, and G. Rivière, 2022: Influence of reduced winter land–sea contrast on the midlatitude atmospheric circulation. *J. Climate*, **35**, 6237–6251, https://doi.org/10.1175/JCLI-D-21-0941.1.

Rahmstorf, S., J. E. Box, G. Feulner, M. E. Mann, A. Robinson, S. Rutherford, and E. J. Schaffernicht, 2015: Exceptional twentieth-century slowdown in Atlantic Ocean overturning circulation. *Nat. Climate Change*, **5**, 475–480, https://doi.org/10.1038/nclimate2554.

Scheff, J., and D. Frierson, 2012: Twenty-first-century multimodel subtropical precipitation declines are mostly midlatitude shifts. *J. Climate*, **25**, 4330–4347, https://doi.org/10.1175/JCLI-D-11-00393.1.

Seager, R., N. Naik, and G. A. Vecchi, 2010: Thermodynamic and dynamic mechanisms for large-scale changes in the hydrological cycle in response to global warming. *J. Climate*, **23**, 4651–4668, https://doi.org/10.1175/2010JCLI3655.1.

——, and Coauthors, 2024: Recent and near-term future changes in impacts-relevant seasonal hydroclimate in the world's Mediterranean climate regions. *Int. J. Climatol.*, **44**, 3792–3820, https://doi.org/10.1002/joc.8551.

Simpson, I. R., T. A. Shaw, and R. Seager, 2014: A diagnosis of the seasonally and longitudinally varying midlatitude circulation response to global warming. *J. Atmos. Sci.*, **71**, 2489–2515, https://doi.org/10.1175/JAS-D-13-0325.1.

——, R. Seager, M. Ting, and T. A. Shaw, 2016: Causes of change in Northern Hemisphere winter meridional winds and regional hydroclimate. *Nat. Climate Change*, **6**, 65–70, https://doi.org/10.1038/nclimate2783.

Stephenson, D. B., and I. M. Held, 1993: GCM response of northern winter stationary waves and storm tracks to increasing amounts of carbon dioxide. *J. Climate*, **6**, 1859–1870, https://doi.org/10.1175/1520-0442(1993)006<1859:GRONWS>2.0.CO;2.

Sutton, R. T., B. Dong, and J. M. Gregory, 2007: Land/sea warming ratio in response to climate change: IPCC AR4 model results and comparison with observations. *Geophys. Res. Lett.*, **34**, L02701, https://doi.org/10.1029/2006GL028164.

Tuel, A., and E. A. B. Eltahir, 2020: Why is the Mediterranean a climate change hot spot? *J. Climate*, **33**, 5829–5843, https://doi.org/10.1175/JCLI-D-19-0910.1.

——, S. Kang, and E. A. Eltahir, 2021a: Understanding climate change over the southwestern Mediterranean using high-resolution simulations. *Climate Dyn.*, **56**, 985–1001, https://doi.org/10.1007/s00382-020-05516-8.

——, P. A. O'Gorman, and E. A. B. Eltahir, 2021b: Elements of the dynamical response to climate change over the Mediterranean. *J. Climate*, **34**, 1135–1146, https://doi.org/10.1175/JCLI-D-20-0429.1.

Wills, R. C. J., and T. Schneider, 2018: Mechanisms setting the strength of orographic Rossby waves across a wide range of climates in a moist idealized GCM. *J. Climate*, **31**, 7679–7700, https://doi.org/10.1175/JCLI-D-17-0700.1.

——, R. H. White, and X. J. Levine, 2019: Northern Hemisphere stationary waves in a changing climate. *Curr. Climate Change Rep.*, **5**, 372–389, https://doi.org/10.1007/s40641-019-00147-6.

Zappa, G., M. K. Hawcroft, L. Shaffrey, E. Black, and D. J. Brayshaw, 2015a: Extratropical cyclones and the projected decline of winter Mediterranean precipitation in the CMIP5 models. *Climate Dyn.*, **45**, 1727–1738, https://doi.org/10.1007/s00382-014-2426-8.

——, B. J. Hoskins, and T. G. Shepherd, 2015b: The dependence of wintertime Mediterranean precipitation on the atmospheric circulation response to climate change. *Environ. Res. Lett.*, **10**, 104012, https://doi.org/10.1088/1748-9326/10/10/104012.

——, P. Ceppi, and T. G. Shepherd, 2020: Time-evolving sea-surface warming patterns modulate the climate change response of subtropical precipitation over land. *Proc. Natl. Acad. Sci. USA*, **117**, 4539–4545, https://doi.org/10.1073/pnas.1911015117.